C. Giordano, F. Topputo
Aeroballistic Capture at Mars: Modeling, Optimization, and Assessment
Journal of Spacecraft and Rockets, Published online 23/03/2022
doi:10.2514/1.A35176

Aero-Ballistic Capture at Mars: Modeling, Optimization, and Assessment

Carmine Giordano*
Politecnico di Milano, Milano, Italy, 20156

Francesco Topputo†
Politecnico di Milano, Milano, Italy, 20156

In this paper a novel paradigm for Mars missions is modeled, optimized, and assessed. This concept consists of a maneuver that combines aerocapture and ballistic capture upon Mars arrival, labelled aero-ballistic capture. The idea is reducing the overall cost and mass by exploiting the interaction with the planet atmosphere as well as the complex Sun–Mars gravitational field. The aero-ballistic capture paradigm is first formulated. This is then split into a number of phases, each of them is modelled with mathematical means. The problem is then stated by using optimal control theory, and optimal solutions are sought. These are specialized to four application cases. An assessment of aero-ballistic capture shows their superiority compared to classical injection maneuvers when medium-to-high final orbits about Mars are targeted.

Nomenclature

a = semi-major axis, km
C_D = drag coefficient
C_L = lift coefficient
c_p = isobaric specific heat capacity, J/(kg K)
e = eccentricity
f = true anomaly, rad
g = gravity acceleration, km/s^2
H = enthalpy, J
h = angular momentum
I_{sp} = specific impulse, s
J_2 = first zonal term

*PostDoc Fellow, Dept. of Aerospace Science and Technology; carmine.giordano@polimi.it.
†Full Professor, Dept. of Aerospace Science and Technology; francesco.topputo@polimi.it. AIAA Senior Member.

M = Mach number

$\mathcal{M}$ = transformation map

m = mass, kg

q = heat load, J/cm^2

$\dot{q}$ = heating rate, W/cm^2

R = planetary radius, km

r = distance, km

r_b = base radius, m

r_n = nose radius, m

S = base surface, m^2

T = temperature, K

V = velocity, km/s

α = frame rotation angle, rad

γ = flight path angle, rad

θ = longitude, rad

μ = mass parameter

μ_i = standard gravitational parameter, km^3/s^2

ρ = density, kg/m^3

σ = bank angle, rad

ϕ = latitude, rad

ψ = heading angle, rad

Ω = planet angular velocity, rad/s

Subscripts

0 = intial time

1, $\odot$ = Sun

2, $\male$ = Mars

atm = atmosphere

int = interface

fin = final time

out = atmospheric exit

TPS = thermal protection system

w = surface wall

I. Introduction

In space exploration, mass has always been a major limiting factor, imposing a very restrictive constraint on missions. Since launch vehicles have limited capability in terms of payload, there is the need of minimizing the launch mass while achieving the scientific goals. Deepening orbital mechanics knowledge to find less fuel-expensive maneuvers is one possible path to fulfill this constraint. In this document, the basic idea is to merge two different approaches, aerocapture and ballistic capture, in order to obtain less fuel consuming and safer trajectories. Mars is selected as case study in this work due to the interest in the scientific and in the space exploration community [1]. Many probes are expected to be sent to Mars in the near future and fuel-optimal trajectories will be needed.

Aerocapture is an orbital maneuver that allows to change the trajectory of a spacecraft from a hyperbolic to an elliptical orbit [2]. This maneuver reduces the amount of propellant needed to go from the hyperbolic approaching up to the final orbit exploiting the friction with the planetary atmosphere. The fuel consumption is reduced and thus, the spacecraft is more efficient. On the other hand, aerocapture needs spacecraft with a capsule-like shape in order to yield appropriate lift-to-drag ratios and a good control authority. A closed-loop guidance has to also be implemented. Furthermore a dedicated thermal protection system (TPS) is required in order to manage the high heat load produced by friction. In the last thirty years, aerocapture has been the subject of some relevant papers [3–5], even if it has never been used in a real mission. Benefits of this technique with respect to a fully propulsive maneuver, both in terms of spacecraft mass and costs, are clearly shown in [6]. In this study, a payload mass increase of 15% is obtained for Martian scenarios. For this reason, this approach was studied for different bodies in the solar system, both for moons [7, 8] and for planets [9, 10]. Aerocapture was analyzed also for re-entry on the Earth [11]. Many studies focused on Mars [12], for the scientific interest about that planet, and also due to the fact that the Mars Sample Return Orbiter, a space mission expected to be launched in 2005 but never performed, was designed to exploit this technique [13]. Since the dynamics related to aerocapture is well known, nowadays effort is put on finding a reliable, accurate and high-performance guidance [2]. Different algorithms were developed, most of them using the bank angle as control command, designed in order to ensure a correct exit condition. These algorithms can be grouped in different categories: analytical predictor-corrector [14, 15], numerical predictor-corrector [16] or terminal point controller [17]. Algorithms using a different control variable were also investigated [18]. Recently, a *closed-loop* optimal aerocapture guidance was developed [2]. It confirms theoretically what was showed numerically in previous studies [19]: if post-atmospheric ΔV minimization is desired, using the bank angle as control, the optimal trajectory has a bang-bang structure, with the vehicle flying nearly full lift up, then almost full lift down.

Ballistic capture is a technique used to reduce the amount of propellant needed to acquire an orbit about a celestial body, which exploits the gravitational accelerations provided on the spacecraft by different celestial bodies at the same time [20]. Indeed, if a spacecraft approaches a body from outside the sphere of influence with low relative velocity, some non-Keplerian low-energy orbits can be found; these allow the spacecraft to temporarily revolve about the planet. The

concept of ballistic capture was first proposed by Belbruno and Miller for Earth to Moon transfer in early 90s [20] and it was later successfully used to rescue the Japanese spacecraft *Hiten*. Since this technique was proven to be effective and efficient, many studies focused their aim in this subject. A method for finding this kind of orbits was devised in order to extend them from the Earth–Moon system to interplanetary trajectories, under the assumption of the *circular restricted three body problem* (CR3BP) [21]. However the classical restricted three body problem is not capable of accurately representing the Solar system dynamics, because the real trajectories of the planets are oversimplified. For this reason, studies on the *elliptic three body problem* (ER3BP) were performed [22, 23]. The method used in these papers to design ballistic capture was then extended to a n-body problem, accurately representing the three-dimensional dynamics of the planetary orbits, through the ephemeris [24]. The effects of natural satellites in ballistic capture was addressed [25]. A summary and a comparison among all these frameworks (circular three-body, elliptic three-body and three-dimensional n-body) can be found in [26]: it is showed that the ER3BP is a good approximation of the real model and it allows to save computational time and effort. Additionally, different studies were performed in order to better understand the effects of planetary relative configuration on the ballistic capture [27–29]. All these different studies produce only temporary orbits about the smaller primary. It was demonstrated that permanent capture by the smaller primary in the R3BP is of no probability [30]. Thus, a stabilization mechanism through dissipation is required, e.g. performing multiple passages in the high atmosphere to exploit aerobraking [31].

Ballistic capture and aerocapture were quite well investigated in previous years, because they are able to improve the efficiency of the interplanetary missions, so reducing the propellant needed to close the orbit and thus increasing the scientific return. These two approaches were studied separately. Firstly, because they are ontologically different and the combination is not trivial. Then, they are possible at different conditions: in case of aerocapture, the spacecraft at Mars arrival is on an hyperbola, with a high excess velocity; on the contrary, for ballistic capture, the vehicle is on lower velocity trajectories. Also the models used are different, considering that a patched conics approach is adopted for aerocapture, while ballistic capture is feasible only under a more complex multi-body problem. Nevertheless, a combination of these two techniques can be beneficial in term of mass with respect to the two approaches taken separately. In fact, for what concerns aerocapture, a merging will possibly reduce the heat and mechanical stresses on the TPS, and this means lower mass for the heat shield. Moreover, the pericenter can be raised by exploiting the Sun perturbation, allowing to perform the propulsive maneuver at the pericenter, and not at the apocenter, reducing the amount of propellant needed thanks to the Oberth effect. On the other hand, a mix of these two *different worlds* can shorten the time of flight compared to a simple ballistic capture.

In this paper, the merging of ballistic capture with aerocapture in order to obtain less fuel-expensive, cheaper and safer trajectories is investigated. The paper is structured as follows. In Section II an overview of both aerocapture and ballistic capture is given. The aero-ballistic capture is modeled in Section III and its optimization, maximizing the scientific return, is discussed in Section IV. Lastly, results and comparisons between this approach and classical methods are

presented in Section V, in order to assess aero-ballistic capture performances with respect to state-of-the-art approaches.

II. Background

A. Aerocapture

1. Vehicle Geometry

In aerocapture, the spacecraft has a capsule-like shape in order to dissipate orbital energy by converting it into thermal energy, while having a good lift-to-drag ratio, and so a good control authority. Furthermore, the heat load is manageable using this shape. Figure 1 shows the vehicle used in this work. The spacecraft is a typical 70-deg-sphere-cone vehicle, commonly used for Mars entry vehicles in the past [12, 32]. Its relevant geometric parameters are the nose radius r_n and the base radius r_b. For this study, the dimensions, together with the mass of the vehicle m_0, are based on the Mars Sample Return Orbiter data [15] and they are summarized in Table 1. The base surface $S = \pi r_b^2$ is taken as reference for the aerodynamic coefficients.

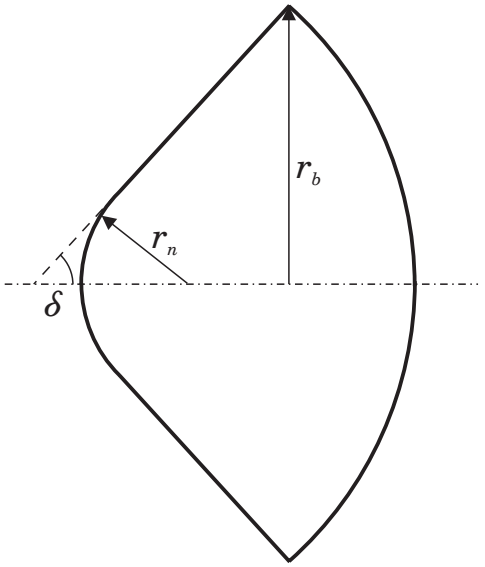

Fig. 1 Capsule shape with relevant parameters

Table 1 Capsule parameters

r_n [m]	r_b [m]	S [m^2]	δ [deg]	m_0 [kg]
0.2013	1.659	8.647	70	2200

2. Equations of motion

If an ellipsoidal rotating planet is considered, the equations of motion of the spacecraft inside the atmosphere can be written using six coupled ODEs, three describing the kinematics and three related to the dynamics. They are [2]

$$\dot{r} = V \sin\gamma \tag{1a}$$

$$\dot{V} = -D - g_r \sin\gamma - g_\phi \cos\gamma \cos\psi + \Omega_{\male}^2 r \cos\phi \left(\sin\gamma \cos\phi - \cos\gamma \sin\phi \cos\psi\right) \tag{1b}$$

$$\dot{\gamma} = \frac{1}{V}\left[L\cos\sigma + \left(\frac{V^2}{r} - g_r\right)\cos\gamma + g_\phi \sin\gamma \cos\psi + 2\Omega_{\male} V \cos\phi \sin\psi \right.$$
$$\left. + \Omega_{\male}^2 r \cos\phi \left(\cos\gamma \cos\phi + \sin\gamma \cos\psi \sin\phi\right)\right] \tag{1c}$$

$$\dot{\theta} = \frac{V \cos\gamma \sin\psi}{r \cos\phi} \tag{1d}$$

$$\dot{\psi} = \frac{1}{V}\left[\frac{L\sin\sigma}{\cos\gamma} + \frac{V^2}{r}\cos\gamma \sin\psi \tan\phi + g_\phi \frac{\sin\psi}{\cos\gamma} \right.$$
$$\left. -2\Omega_{\male} V \left(\tan\gamma \cos\psi \cos\phi - \sin\phi\right) + \frac{\Omega_{\male}^2 r}{\cos\gamma} \sin\psi \sin\phi \cos\phi\right] \tag{1e}$$

$$\dot{\phi} = \frac{V \cos\gamma \cos\psi}{r} \tag{1f}$$

where r is the distance from the planet center, V the velocity, γ the flight path angle, θ and ϕ the longitude and the latitude, while ψ is the heading angle of the velocity vector, measured clockwise from the north in the local horizontal plan; σ is the bank angle. By definition, this is the angle of rotation of the vehicle about the velocity vector, positive with the right wing down. L and D are the lift and drag accelerations, i.e.,

$$L = \frac{1}{2}\rho V^2 S \frac{C_L}{m_0} \tag{2}$$

$$D = \frac{1}{2}\rho V^2 S \frac{C_D}{m_0} \tag{3}$$

The density ρ is a function of r. Since the simple exponential model for the air density is not capable of giving the desired accuracy, the model suggested by Justus [33] is implemented. It is based on the Committee on Space Research (COSPAR) Mars Reference Atmosphere [34]: values of density, temperature and pressure are tabulated for different altitudes; a spline interpolation with not-a-knot end conditions is used to connect the different points, in order to have a C^2-class function. The interface for Mars atmosphere is set at an altitude of 125 km. The aerodynamics coefficients C_L and C_D are dependent on the angle of attack. Usually, in these problems, the angle of attack is function of the Mach number. In aerocapture, the Mach number is high and the motion is considered fully hypersonic. For this reason, these coefficients are considered constant. For a capsule-like vehicle, $C_D = 1.723$ and the ratio $C_L/C_D = 0.27$[15].

The planet angular velocity is indicated with the symbol $\Omega_{\male}$. The terms g_r and g_ϕ are the gravity accelerations, respectively in radial and lateral direction. If a planet with the zonal term J_2 dominating the other ones is considered, they can be written in an approximate form as [35]

$$g_r = \frac{\mu_{\male}}{r^2}\left[1 + \frac{3}{2}J_2\left(\frac{R}{r}\right)^2\left(1 - 3\sin^2\phi\right)\right]$$

$$g_\phi = \frac{\mu_{\male}}{r^2}\left[3J_2\left(\frac{R}{r}\right)^2\left(3\sin\phi\cos\phi\right)\right]$$

where $\mu_{\male}$ is the standard gravitational parameter of Mars and R is the equatorial radius of the planet.

The equations of motion for the atmospheric phase can be simplified making some assumptions. First of all, since the atmospheric phase of the aerocapture maneuver lasts only few minutes, the rotation of the planet can be neglected. Also the non-spherical gravity can be ignored due to its small magnitude, since $J_2 = 1.960 \times 10^{-3}$.

Under these assumptions, the equations of motion become

$$\dot{r} = V\sin\gamma \tag{4a}$$

$$\dot{V} = -D - \frac{\mu_{\male}}{r^2}\sin\gamma \tag{4b}$$

$$\dot{\gamma} = \frac{1}{V}\left[L\cos\sigma + \left(V^2 - \frac{\mu_{\male}}{r}\right)\frac{\cos\gamma}{r}\right] \tag{4c}$$

$$\dot{\theta} = \frac{V\cos\gamma\sin\psi}{r\cos\phi} \tag{4d}$$

$$\dot{\phi} = \frac{V\cos\gamma\cos\psi}{r} \tag{4e}$$

$$\dot{\psi} = \frac{1}{V}\left[\frac{L\sin\sigma}{\cos\gamma} + \frac{V^2}{r}\cos\gamma\sin\psi\tan\phi\right] \tag{4f}$$

Eqs. (4a), (4b), and (4c), describing the longitudinal dynamics, are decoupled from the other three equations, describing the lateral dynamics. For this reason, the in-plane trajectory can be studied separately from the out-of-plane one.

B. Heating rates model

In aerocapture, the orbital energy is dissipated converting it into thermal energy, thanks to the interaction with the atmosphere. For this reason, heating rates represent one of the major issues. For capsule-like vehicles, only the stagnation heating rate is considered, both radiative and convective [36], that is

$$\dot{q} = \dot{q}_{\text{conv}} + \dot{q}_{\text{rad}} \tag{5}$$

The convective stagnation point heating rate is computed using the Marvin–Deiwert model [37]

$$\dot{q}_{\text{conv}} = k_0 \left(\frac{\rho}{r_n}\right)^{\frac{1}{2}} V^{3.04} \left(1 - \frac{h_w}{H}\right) \tag{6}$$

with k_0 a constant, equal to 1.35×10^{-8} for Mars, h_w the wall enthalpy, and H the total enthalpy. Assuming to have radiative equilibrium, the latter are computed as

$$h_w = c_{p_{\text{TPS}}} T_w \qquad \text{with} \quad T_w = \left(\frac{\dot{q}}{\sigma_{SB}\varepsilon}\right)^{\frac{1}{4}}$$

and

$$H = c_{p_{\text{atm}}} T_{\text{atm}} \left(1 + \frac{\gamma_{\text{atm}} - 1}{2} M^2\right)$$

where σ_{SB} the Stefan–Boltzmann constant, ε the TPS surface emissivity, T_{atm} the atmospheric temperature given by the atmosphere model and $M = V/\sqrt{\gamma_{\text{atm}} R_{\text{atm}} T_{\text{atm}}}$ is the Mach number.

The radiative stagnation point heating rate is computed using the Tauber–Sutton model [38]

$$\dot{q}_{\text{rad}} = C r_n^a \rho^b f(V) \tag{7}$$

For the Martian environment, the constants in Eq. (7) are

$$C = 2.35 \times 10^{-4}, \quad a = 0.526 \quad \text{and} \quad b = 1.19$$

Instead, $f(V)$ is a tabulated value dependent on velocity [38]. Both the relations (6) and (7) give results in W/cm^2. Starting from Eq. (5) and (6), it can be seen that the total heating rate $\dot{q}$ is described by an implicit function.

In the equations describing the heat loads, thermal and optical properties of the TPS are needed. Since in the atmospheric phase, the heating rate is expected to be the same of previous studies on Mars, an ablative TPS is chosen [32]. Among the different ablative material, SLA-561V is selected. Produced by Lockheed Martin *, it is a widespread technology for 70deg sphere-cone vehicle for Mars missions. SLA-561V is characterized by $c_{p_{\text{TPS}}} = 1260\ \text{J kg}^{-1}\ \text{K}^{-1}$ and $\varepsilon = 0.97$.

The last point related to TPS is the estimation of its mass. This is of paramount importance for the following mass optimization. As shown in [39], historical data on previous NASA missions give a direct relation between the TPS mass fraction and the integrated total heat load q (Figure 2). Basing on this connection, the mass of the TPS is estimated

*Lockheed-Martin, SLA-561 Product Informations, Retrieved on: 2021/05/18

using the formula given by the fit curve in Figure 2 (in blue), whose analytic expression is

$$\frac{m_{\mathrm{TPS}}}{m_0} = K q^{\beta} \tag{8}$$

with $K = 0.091$ and $\beta = 0.51575$.

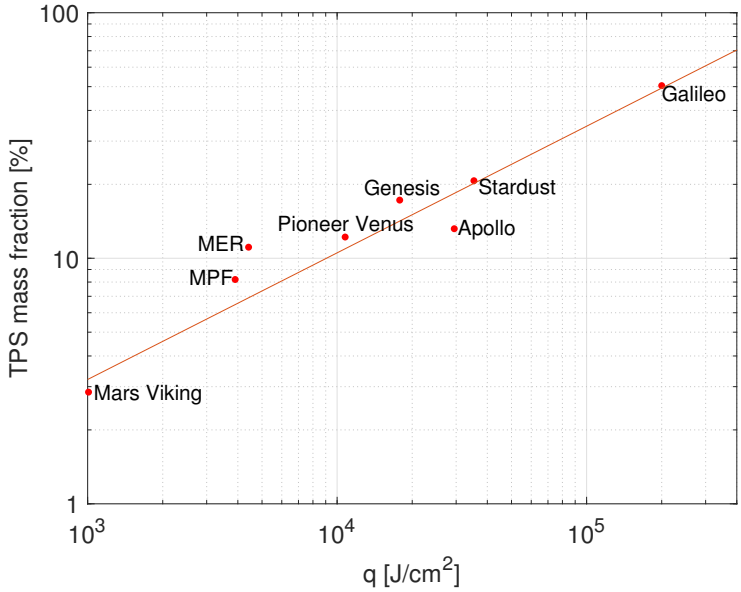

Fig. 2 TPS mass fraction and total heat load for previous missions with ablative heat shield [39]

C. Ballistic capture

1. Equations of motion

If ballistic capture is considered, the two-body problem cannot is not suitable. For this reason, more complex, but accurate models, have to be implemented. The *Elliptic Restricted Three-Body problem* (ER3BP) is a generalization of the *Circular Restricted Three-Body problem* (CR3BP), which is deeply analyzed in literature. This problem studies the planar motion of a third massless body P, attracted by two primaries, P_1 and P_2, of mass m_1 and m_2 respectively, revolving one around the other in an elliptic motion.The elliptic problem describes quite accurately the dynamics of the Solar System[26]. For this reason together with the fact that Mars orbit eccentricity is not negligible (~ 0.1), this model is used for the extra-atmospheric phase.

A non-uniformly rotating, barycentric, adimensional reference frame ($\hat{\xi}$, $\hat{\eta}$, $\hat{h}$), called *synodic frame*, is defined in order to write the equation of motion for P. The center of this system is placed at the primaries barycenter; the $\hat{\xi}$ axis is aligned with the two primaries, with $\hat{h}$ orthogonal to the plane of motion. In this frame, P_1 and P_2 have fixed position ($-\mu$, 0) and ($1-\mu$, 0) respectively, with $\mu = m_2/(m_1 + m_2)$, being the mass parameter of the system (see Figure 3). Moreover,

the distances are normalized accordingly to the distance between P_1 and P_2.

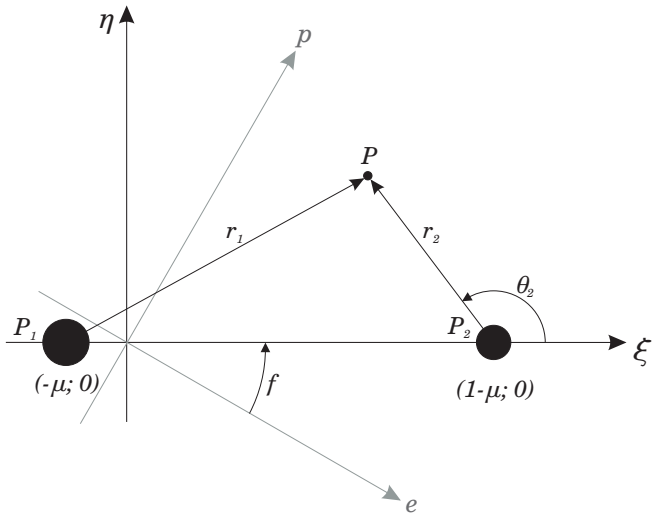

Fig. 3 Rotating, pulsating, non-inertial reference frame with polar coordinates. The inertial sidereal perifocal reference frame is drawn in gray.

Defining e_p the eccentricity of the ellipses described by the two primaries around the barycenter, the unit distance can be defined as

$$r_{\text{ref}} = \frac{a_p(1-e_p^2)}{1+e_p\cos f}$$

where f is the true anomaly of the system and a_p the primary semi-major axis. Therefore, r_{ref} varies in time according to the mutual position of the two primaries, so creating a pulsating reference system.

The true anomaly f represents the independent variable of the system, playing the role of the time, making the system non-autonomous. If the period of revolution of the system $P_1 - P_2$ is set equal to 2π and a_p is set to the unity, the link between f and time can be written in differential form as

$$\frac{\mathrm{d}f}{\mathrm{d}t} = \frac{\left(1+e_p\cos f\right)^2}{\left(1-e_p^2\right)^{3/2}} \tag{9}$$

In this framework, it is possible to write the equations of motion for the third body as [40]

$$\begin{aligned} \xi'' - 2\eta' &= \omega_\xi \\ \eta'' + 2\xi' &= \omega_\eta \end{aligned} \tag{10}$$

with the primes representing the derivatives with respect to f and the subscripts the partial derivatives of

$$\omega(\xi,\eta,f) = \frac{\Omega(\xi,\eta)}{1+e_p\cos f} \tag{11}$$

where Ω is the potential function, defined as

$$\Omega(\xi,\eta) = \frac{1}{2}(\xi^2+\eta^2) + \frac{1-\mu}{r_1} + \frac{\mu}{r_2} + \frac{1}{2}\mu(1-\mu) \tag{12}$$

and $r_1 = \sqrt{(\xi+\mu)^2+\eta^2}$ and $r_2 = \sqrt{(\xi+\mu-1)^2+\eta^2}$ are the distances of P from the primaries.

For the Sun–Mars three-body problem used in this work, the main parameters are presented in Table 2. Beside the synodic reference frame, the three body problem can be described using polar coordinates, centered at P_2. If r_2 is defined as the magnitude of the vector from P_2 to the third body and θ_2 is the angle between the $\hat{\xi}$ axis and this vector (see Figure 3), P moves under the dynamics described by [22]

$$\begin{aligned} r_2'' - r_2\theta_2'^2 - 2r_2\theta_2' &= \frac{1}{1+e_p\cos f}\left[r_2\left(1-\frac{1-\mu}{r_1^3}\right) - \frac{\mu}{r_2^2} + (1-\mu)\cos\theta_2\left(1-\frac{1}{r_1^3}\right)\right] \\ r_2\theta_2'' + 2r_2'\theta_2' + 2r_2' &= \frac{(1-\mu)\sin\theta_2}{1+e_p\cos f}\left(\frac{1}{r_1^3}-1\right) \end{aligned} \tag{13}$$

with $r_1 = \sqrt{r_2^2 + 2r_2\cos\theta_2 + 1}$. Since these equations involve trigonometric functions, they are computational expensive, but they allow easier writing of terminal conditions and they are able to provide a smooth function for $\theta_2 = \theta_2(f)$.

Table 2 Sun–Mars Three-Body problem parameters

μ [-]	a_p [AU]	e_p [-]
3.226208×10^{-7}	1.523688	0.093418

2. Sun gravitational assist

In order to better understand the dynamics of the spacecraft when it is subjected to natural dynamics, the effects of the Solar gravity field near to Mars are investigated. At first, the solar gravity gradient field near Mars is analyzed, without taking into account the presence of the planet. Referring to Figure 4, the definition of the gravity acceleration is

$$\mathbf{g}_\odot = \frac{\mu_\odot}{\left\|\mathbf{R}_\odot - \mathbf{r}_2\right\|^3}\begin{bmatrix}\left(\mathbf{R}_\odot - \mathbf{r}_2\right)\cdot\hat{x} \\ \left(\mathbf{R}_\odot - \mathbf{r}_2\right)\cdot\hat{y}\end{bmatrix} \tag{14}$$

then neglecting the higher order terms, the gradient can be defined as [27]

$$\nabla\mathbf{g}_\odot = \begin{bmatrix}\frac{\partial}{\partial x}(\mathbf{g}_\odot\cdot\hat{x}) \\ \frac{\partial}{\partial y}(\mathbf{g}_\odot\cdot\hat{y})\end{bmatrix} = \frac{\mu_\odot}{R_\odot^3}\begin{bmatrix}\left(3\hat{R}_{\odot_x}^2 - 1\right)x \\ \left(3\hat{R}_{\odot_y}^2 - 1\right)y\end{bmatrix} \tag{15}$$

where $\hat{R}_{\odot_x} = (\mathbf{R}_\odot \cdot \hat{x})/\|\mathbf{R}_\odot\|$ and $\hat{R}_{\odot_y} = (\mathbf{R}_\odot \cdot \hat{y})/\|\mathbf{R}_\odot\|$.

The Sun gravity gradient vector field is showed in Figure 5(a), where the length of the arrows is proportional to its strength. It is shown that the further the third body is from the planet, the strongest is the effect of the Sun, but for different angular positions with respect to Mars, a diverse effect is attained, since the field lines change direction. For exemple, considering prograde orbits, if the apocenter is in the second or fourth quadrant, an increase in orbital energy or angular momentum is obtained, since the tangential component of the gravity force and the tangential velocity point to the same direction; otherwise, in the first and third quadrant, the Sun gravity slows down the vehicle, dissipating its orbital energy (Figure 5(b)).

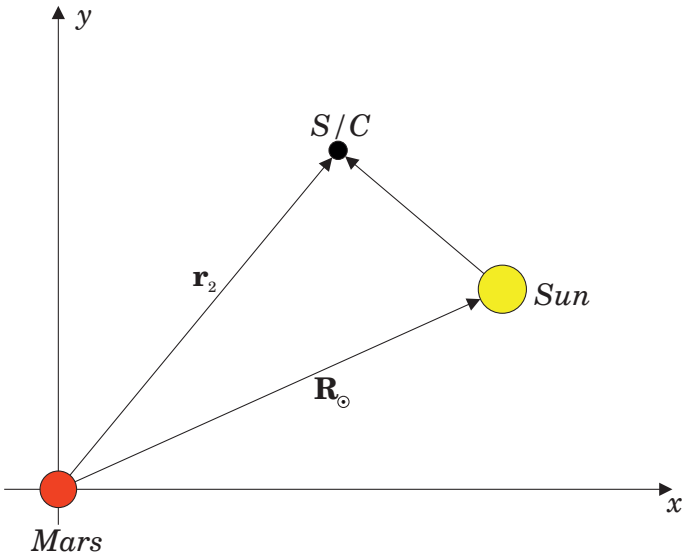

Fig. 4 Solar gravity gradient reference figure.

For the ER3BP, the distance of Mars with respect to the Sun varies in time, so $R_\odot$ is not a constant. It is

$$R_\odot = \frac{a_p\left(1 - e_p^2\right)}{1 + e_p \cos f} \tag{16}$$

and a dependence from true anomaly appears. Since this quantity is at the denominator, the solar influence is the strongest when $(1 + e_p \cos f)$ is the highest. Thus, the solar gravitational assist is more effective across the pericenter of the Sun–Mars orbit, when the cosine function has its maximum.

The same effect can be studied by analyzing the change in angular momentum, as showed in [29]. Indeed, it is possible to write the position and the velocity of a body in non-inertial P_2-centered frame as

$$\mathbf{r} = \begin{bmatrix} r_\xi \\ r_\eta \end{bmatrix} = \begin{bmatrix} r_2 \cos(\theta_2) \\ r_2 \sin(\theta_2) \end{bmatrix} \tag{17}$$

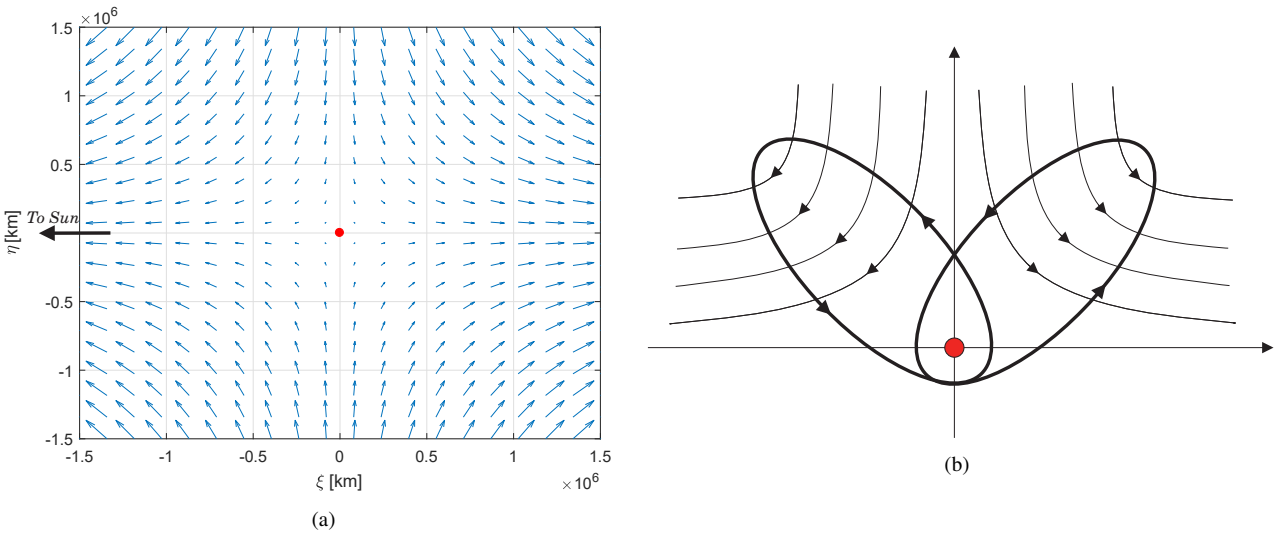

Fig. 5 (a) Solar gravity gradient field lines near Mars. The dot indicates Mars position. (b) Solar gravity gradient field effect on orbits near Mars.

$$\mathbf{v} = \begin{bmatrix} v_\xi \\ v_\eta \end{bmatrix} = \begin{bmatrix} r_2' \cos(\theta_2) - r_2\theta_2' \sin(\theta_2) \\ r_2' \sin(\theta_2) + r_2\theta_2' \cos(\theta_2) \end{bmatrix} \tag{18}$$

Now, two rotation matrices and two reference quantities can be described. They are, respectively,

$$T_f = \begin{bmatrix} \cos f & -\sin f \\ \sin f & \cos f \end{bmatrix}, \qquad T_f' = \begin{bmatrix} -\sin f & -\cos f \\ \cos f & -\sin f \end{bmatrix}$$

and

$$r_f = \frac{1 - e_p^2}{1 + e_p \cos f}, \qquad r_f' = \frac{(1 - e_p^2) e_p \sin f}{(1 + e_p \cos f)^2}$$

Recalling the link between time and true anomaly given by Eq. (9), it is possible to define the state in inertial P_2-centered reference frame computing

$$\mathbf{R} = r_f T_f \mathbf{r} \tag{19}$$

$$\mathbf{V} = \frac{\mathrm{d}f}{\mathrm{d}t} \left[r_f T_f \mathbf{v} + \left(r_f' T_f + r_f T_f' \right) \mathbf{r} \right] \tag{20}$$

In conclusion, the angular momentum respect to P_2, expressed as a scalar, since a planar motion is considered can be evaluated through

$$h_{P_2} = \|\mathbf{R} \times \mathbf{V}\| \tag{21}$$

and so, for the elliptic problem, it reads

$$h_{P_2} = \sqrt{(1-e_p^2)}\left(r_2^2 + r_2^2\theta_2'\right) \tag{22}$$

It is possible to compute the variation of h_{P_2} deriving it with respect to time, finding that

$$\dot{h}_{P_2} = \frac{\mathrm{d}h}{\mathrm{d}f}\frac{\mathrm{d}f}{\mathrm{d}t} = \sqrt{(1-e_p^2)}\left(2r_2r_2' + 2r_2r_2'\theta_2' + r_2^2\theta_2''\right)\frac{\mathrm{d}f}{\mathrm{d}t} \tag{23}$$

Using Eq. (13) together with Eq. (9), it can be written that

$$\dot{h}_{P_2} = r_2(1-\mu)\sin\theta_2\left[\frac{1}{\left(r_2^2 + 2r_2\cos\theta_2 + 1\right)^{3/2}} - 1\right]\frac{1+e_p\cos f}{1-e_p^2} \tag{24}$$

In Figure 6, the adimensional angular momentum variation is plotted with $e_p = 0$. Also in this case, an increase in angular momentum can be found in the second and in the fourth quadrant. In those locations, h_{P_2} increases, which means that the semi-major axis with respect to the smaller primary increases, or equivalently the eccentricity is reduced. If orbits close to P_2 are considered, only the second effect has a major importance. Thus, if the apocenter of an orbit around P_2 is in the second or in the fourth quadrant, a raising in the pericenter is expected. Instead, considering the relative positions of the primaries, the angular momentum has its maximum when $f = 0$ and the solar gravity assist is the strongest when the two primaries are as close as possible.

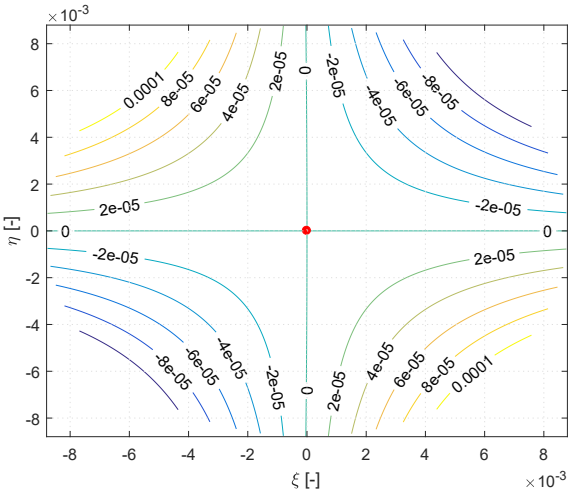

Fig. 6 Adimensional angular momentum variation near Mars. The dot indicates Mars position. Positive values only in II and IV quadrant.

III. The Aero-Ballistic Capture

A. Aero-Ballistic Capture Paradigm

With reference to Figure 7, the strategy used to merge aerocapture with ballistic capture is defined as:

1) Initially, the spacecraft approaches Mars with an hyperbolic trajectory with pericenter inside the atmosphere;
2) The probe passes through the atmosphere and some orbital energy is dissipated by aerodynamic drag and converted into heat;
3) At the exit, at the atmospheric interface, the vehicle is on a closed orbit, but with a high apocenter, such that the effects of solar gravity cannot be neglected;
4) The Sun gravity field accelerates the probe when it is far from Mars and, thus, the pericenter is naturally raised and taken out from the atmosphere, at the desired altitude, if the geometrical conditions are verified;
5) Finally, at the pericenter of this intermediate orbit, a propelled impulse is applied in order to reduce the velocity and thus lowering the apocenter to a prescribed value.

Figure 7 shows the different phases of the aero-ballistic capture. It can be divided into four phases:

1) *Approaching phase*: the spacecraft arrives at target planet on an incoming hyperbola;
2) *Atmospheric phase*: the spacecraft is on a controlled trajectory inside the atmosphere;
3) *Ballistic phase*: the spacecraft is on a ballistic, low-energy orbit with a high apocenter;
4) *Final orbit*: the spacecraft is on its target orbit.

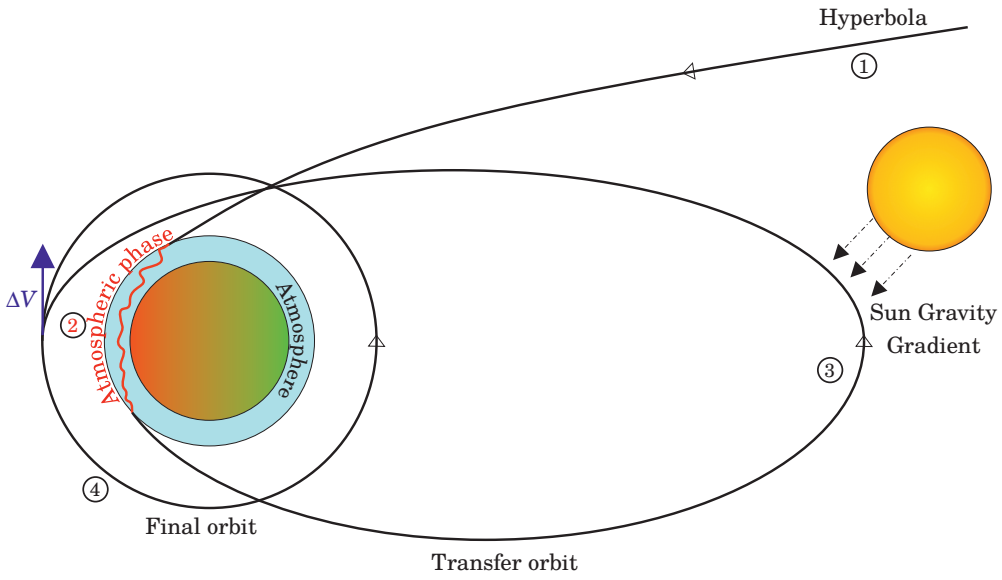

Fig. 7 The four phases of aero-ballistic capture.

In principle, this strategy may allow potential mass savings, since the passage through the atmosphere dissipates less energy than aerocapture, thus, the TPS is lighter. Moreover, the propelled maneuver is performed at the pericenter, and not at the apocenter, and this reduces the fuel consumption thanks to the Oberth effect. On the other hand, this

maneuver reduces the time-of-flight with respect to the ballistic capture and provides a simple stabilization mechanism.

B. Modeling

1. Approaching phase

In this leg, high-energy orbits are involved, so the decomposition of the Solar System in two-body problems is possible. The spacecraft is on an hyperbola that is described using state variables at the atmospheric boundary. Taking as reference previous studies about aerocapture at Mars [12], a $V_0 = 5900$ m s^{-1} and a $\gamma_0 = -9.7$ deg are chosen, where the subscript 0 is used to indicate the interface conditions with Mars atmosphere.

2. Atmospheric phase

Right after the interface, the atmospheric phase begins and it ends when $r(t_{\text{out}}) = r_{\text{int}}$. During this leg, the only controlled one, the dynamics of the vehicle is described by the differential equations (4a)–(4c). In this study, the lateral dynamics is not considered and no orbital inclination target is implemented. Also no guidance algorithm is considered since it is beyond the scopes of this work. The spacecraft is assumed to be always on the Mars orbital plane at the exit from the atmosphere and the bank reversal is considered to occur instantaneously.

For this problem, thermal loads should be accounted and, for this reason, the heating rate, described by the implicit equation (Eqs. (5)–(7))

$$\dot{q} = k_0 \left(\frac{\rho}{r_n}\right)^{\frac{1}{2}} V^{3.04} \left(1 - \frac{c_{pTPS}\left(\frac{\dot{q}}{\sigma_{SB}\varepsilon}\right)^{\frac{1}{4}}}{H}\right) + C r_n^a \rho^b f(V) \tag{25}$$

is added to the ODEs system (4a)–(4c). This equation depends on position and velocity inside the atmosphere, but does not influence the other variables. Thus, in principles, it can be integrated a-posteriori. For this phase to define an augmented state vector $\mathbf{x} = [r,\ V,\ \gamma,\ q]$ is defined.

3. Ballistic phase

In the ballistic phase, after the passage through the atmosphere, the spacecraft is on an orbit under natural dynamics. Since the probe follows a low energy trajectory, the two-body problem no longer represent correctly the equations of motion. For this reason, the ER3BP, given by Eq. (13), is used to describe the dynamics, with the Sun and Mars as primaries. The initial conditions for the ballistic phase are the final conditions of the atmospheric phase and a conversion between them is required. From now on, capital letters are associated to perifocal dimensional reference frame. Conversely lower case letters indicate quantities in non-inertial reference frame.

First of all, position and velocity have to be placed in a Mars-centered inertial frame, since from the first integration only the magnitude of this quantities are computed. Defining α as the angle between the ER3BP perifocal axis and the

spacecraft position vector at the end of the atmospheric phase (see Figure 8), the state of the probe can be defined as

$$\mathbf{R} = \begin{bmatrix} R_{e'} \\ R_{p'} \end{bmatrix} = \begin{bmatrix} r(t_{\text{out}}) \cos\alpha \\ r(t_{\text{out}}) \sin\alpha \end{bmatrix}, \qquad \mathbf{V} = \begin{bmatrix} V_{e'} \\ V_{p'} \end{bmatrix} = \begin{bmatrix} V(t_{\text{out}}) \cos\left(\alpha + \gamma(t_{\text{out}}) - \pi/2\right) \\ V(t_{\text{out}}) \sin\left(\alpha + \gamma(t_{\text{out}}) - \pi/2\right) \end{bmatrix} \tag{26}$$

with r, V and γ the state variables in the previous phase and t_{out} the time at the exit from the atmosphere. The final conditions for the ballistic phase is the pericenter of the intermediate orbit, i.e.,

$$\begin{cases} r_2'\left(f_{\text{fin}}\right) = -\frac{r_2 e_p \sin f_{\text{fin}}}{1+e_p \cos f_{\text{fin}}} \\ r_2''\left(f_{\text{fin}}\right) < 0 \end{cases} \tag{27}$$

with f_{fin} that is the final true anomaly for the primaries. The first final condition represents the condition at an apsis, while the second one allows to select the pericenter (and not the apocenter).

Then a *scaling* is performed, dividing the positions by a_p and the velocities by $\sqrt{\mu_\odot / a_p}$, that is the first cosmic velocity

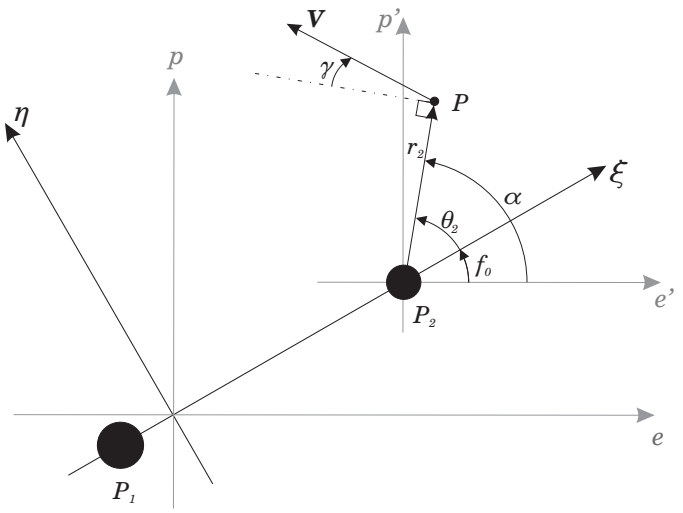

Fig. 8 Definition of α and initial true anomaly f_0. Synodic (in black) and perifocal (in grey) frames are reported.

for an orbit of radius a_p around the Sun. Defining f_0 as the true anomaly when the spacecraft exits the atmosphere, the conversion from the Mars-centered inertial perifocal reference frame to the synodic frame requires two rotation matrices and two reference quantities, the firsts for the positions and the others for the velocities. They are, respectively

$$T_f = \begin{bmatrix} \cos f_0 & -\sin f_0 \\ \sin f_0 & \cos f_0 \end{bmatrix}, \qquad T_f' = \begin{bmatrix} -\sin f_0 & -\cos f_0 \\ \cos f_0 & -\sin f_0 \end{bmatrix}$$

and

$$r_f = \frac{1-e_p^2}{1+e_p\cos f_0}, \qquad r_f' = \frac{(1-e_p^2)e_p\sin f_0}{(1+e_p\cos f_0)^2}$$

Recalling the link between time and true anomaly given by Eq. (9), the state in synodic frame can be computed as

$$\mathbf{r} = \begin{bmatrix} r_\xi \\ r_\eta \end{bmatrix} = \frac{1}{r_f} T_f^T \mathbf{R} - \begin{bmatrix} \mu - 1 \\ 0 \end{bmatrix} \tag{28}$$

$$\mathbf{v} = \begin{bmatrix} v_\xi \\ v_\eta \end{bmatrix} = \frac{1}{r_f} T_f^T \left[\left(\frac{\mathrm{d}f}{\mathrm{d}t} \right)^{-1} \mathbf{V} - \left(T_f r_f' + T_f' r_f \right) \left(\mathbf{r} + \begin{bmatrix} \mu - 1 \\ 0 \end{bmatrix} \right) \right] \tag{29}$$

As last point, conversion form Cartesian coordinates to polar coordinates is needed. Thus, in conclusion, the initial conditions for ER3BP for ballistic phase are retrieved from the final conditions of atmospheric phase writing

$$\begin{aligned} r_2(f_0) &= \sqrt{(r_\xi + \mu - 1)^2 + r_\eta^2} \\ \theta_2(f_0) &= \operatorname{atan2}\left(\frac{r_\eta}{r_2}, \quad \frac{r_\xi + \mu - 1}{r_2} \right) \\ r_2'(f_0) &= v_\xi \cos\theta_2 + v_\eta \sin\theta_2 \\ \theta_2'(f_0) &= \frac{1}{r_2}\left(v_\eta \cos\theta_2 - v_\xi \sin\theta_2 \right) \end{aligned} \tag{30}$$

Since the spacecraft is subjected to pure natural dynamics, the vehicle follows a predetermined path, given the initial conditions. For this reason, it can be convenient to describe the conversions and the integration associated to this leg using a map $\mathcal{M}$. This function takes as inputs the atmosphere exit conditions $(r,\ V,\ \gamma)$ plus the parameters f_0 and α; uses them to find the state in Mars-centered polar coordinates in synodic reference frame; then integrates from f_0 up to the true anomaly f_{fin} when the conditions in Eq. (27) are found; so, the pericenter velocity conditions are directly implemented in the map. Using backward this algorithm, the outputs, that are position and velocity at the end of integration in Mars-centered inertial coordinates, are retrieved. A wrap-up scheme for this map is:

$$\begin{bmatrix} r \\ V \\ \gamma \end{bmatrix}_{t_{\text{out}}} \xmapsto{\alpha} \begin{bmatrix} \mathbf{R} \\ \mathbf{V} \end{bmatrix}_{t_{\text{out}}} \xmapsto{f_0} \begin{bmatrix} \mathbf{r} \\ \mathbf{v} \end{bmatrix}_{f_0} \longmapsto \begin{bmatrix} r_2 \\ r_2' \\ \theta_2 \\ \theta_2' \end{bmatrix}_{f_0} \xmapsto{\int} \begin{bmatrix} r_2 \\ r_2' \\ \theta_2 \\ \theta_2' \end{bmatrix}_{f_{\text{fin}}} \longmapsto \begin{bmatrix} \mathbf{r} \\ \mathbf{v} \end{bmatrix}_{f_{\text{fin}}} \xmapsto{f_{\text{fin}}} \begin{bmatrix} \mathbf{R} \\ \mathbf{V} \end{bmatrix}_{t_{\text{fin}}}$$

In conclusion, it is possible to write

$$\begin{bmatrix} \mathbf{R} \\ \mathbf{V} \end{bmatrix}_{t_{\text{fin}}} = \mathcal{M}_{\alpha,\ f_0}\left(r,\ V,\ \gamma\right)_{t_{\text{out}}} \tag{31}$$

where $\mathcal{M}_{\alpha,\ f_0}$ is the map between the conditions at atmospheric interface and the perifocal dimensional state.

4. Circularization maneuver

After the maneuver at pericenter, a desired closed orbit around the planet is obtained. Since this orbit has a high energy and it is relatively close to Mars, a simple two-body problem, with Mars as primary, is considered. This means that it is possible to compute the pericenter velocity of this final orbit writing

$$v_p^* = \sqrt{2\mu_{\text{♂}}}\sqrt{\frac{1}{r_p^*} - \frac{1}{r_p^* + r_a^*}} \tag{32}$$

where r_p^* is the desired final pericenter and r_a^* is the desired final apocenter.
Starting from this, since $\mathbf{V}(t_{fin})$ is tangential to the orbit by construction, the needed maneuver impulse is

$$\Delta V = v_p^* - \|\mathbf{V}\left(t_{\text{fin}}\right)\| \tag{33}$$

IV. Optimization of Aero-Ballistic Capture

A. Objective function

The *optimal problem* for the aero-ballistic capture maximizes the mass delivered in the final orbit, m_{fin}. The objective function whose minimum is sought is then

$$J = -m_{\text{fin}} \tag{34}$$

Two discrete events contribute to change in the mass value: 1) Ejection of the TPS; 2) Engine burn needed to go to the final orbit. Thus, defining m_{out} as the mass of the spacecraft when the heat shield is jettisoned, it is possible to write

$$m_{\text{fin}} = m_0 \frac{m_{\text{out}}}{m_0} \frac{m_{\text{fin}}}{m_{\text{out}}} \tag{35}$$

where m_0 is the initial mass. Recalling Eq. (8) and Tsiolkovsky rocket equation, since $m_{\text{out}} = m_0\left(1 - \frac{m_{\text{TPS}}}{m}\right)$,

$$J = -m_{\text{fin}} = m_0\left[1 - Kq^{\beta}\left(t_{\text{out}}\right)\right] e^{-\frac{\Delta V}{I_{\text{sp}} g_0}}. \tag{36}$$

B. Statement of the problem

Since the state is $\mathbf{x} = [r,\ V,\ \gamma,\ q]$, for aero-ballistic capture, the optimal problem is to minimize the cost function

$$J = J(\mathbf{x}(t_{\text{out}}), \alpha, f_0)$$

described by Eq. (36), such that

$$\|\mathbf{R}\,(t_{\text{fin}})\| = r_p^* \tag{37}$$

and with where $\Delta V = v_p^* - \|\mathbf{V}\,(t_{\text{fin}})\|$ and $[\mathbf{R},\ \mathbf{V}]_{t_{\text{fin}}}^T = \mathcal{M}_{\alpha,\ f_0}\,(r,\ V,\ \gamma)_{t_{\text{out}}}$, and v_p^* is the velocity at the pericenter of the final orbit. State is subjected to the dynamics system $\dot{\mathbf{x}} = \mathbf{f}(\mathbf{x})$ given by Eqs. (4a)–(4c) and (25) with the bank-angle σ as control variable, subjected to magnitude constraints $0 \leq \sigma_{min} \leq |\sigma| \leq \sigma_{max} \leq \pi$.

In [41], Pontryagin describes how to deal with problems with the cost function dependent not only on the state, but also on some constant parameters. In this case, a conversion from the Problem of Mayer to the Problem of Lagrange is needed [42]. That is

$$J = \varphi\,(\mathbf{x}(t_{\text{out}}),\ \alpha,\ f_0) \quad \rightarrow \quad J = \int_{t_0}^{t_{\text{out}}} \frac{\mathrm{d}\varphi}{\mathrm{d}t}\,\mathrm{d}t \quad \text{with } \varphi\,(\mathbf{x}(t_0),\ \alpha,\ f_0) = 0 \tag{38}$$

An augmented state vector is then defined as

$$\tilde{\mathbf{x}} = [\varphi,\ \mathbf{x}]^T \tag{39}$$

allowing to define the Hamiltonian of the problem as

$$H = \lambda_0 \dot{\varphi} + \boldsymbol{\lambda}^T \mathbf{f} \tag{40}$$

Therefore, by Maximum Principle the optimal bank angle can be found solving

$$\begin{aligned} \sigma = \arg\max \Bigg[& \lambda_0 \frac{\mathrm{d}\varphi}{\mathrm{d}t} + \lambda_r V \sin\gamma + \lambda_V \left(-D - \frac{\mu_{\sigma^{\prime}} \sin\gamma}{r^2} \right) + \\ & + \lambda_\gamma \left(\frac{L}{V} \cos\sigma + \left(V^2 - \frac{\mu_{\sigma^{\prime}}}{r} \right) \frac{\cos\gamma}{rV} \right) + \lambda_q f_q \Bigg] \end{aligned} \tag{41}$$

with f_q the local explicit function associated to the heat load dynamics. It cannot be written explicitly, but its existence can be proven using the *implicit function theorem*.

Since L/V is always positive and $\cos\sigma$ has a monotonic behavior in the interval $[\sigma_{\text{min}},\ \sigma_{\text{max}}] \in [0,\ \pi]$, the optimal

bank angle is determined only by the sign of λ_γ; so

$$\sigma^* = \begin{cases} \sigma_{\min} & \text{if } \lambda_\gamma > 0 \\ \sigma_{\max} & \text{if } \lambda_\gamma < 0 \\ \in [\sigma_{\min},\ \sigma_{\max}] & \text{if } \lambda_\gamma = 0 \text{ in } [t_1,\ t_2] \end{cases} \tag{42}$$

The last case in Eq. (42) is called *singular optimal control*. If that condition is verified, the bank angle can assume a time-varying value in the interval $[\sigma_{\min},\ \sigma_{\max}]$. Otherwise, the control variable can be only $\sigma_{\max}$ or $\sigma_{\min}$ alternatively and so the control has a bang-bang structure. However, it is possible to prove that the singular optimal control is not possible for aero-ballistic capture (see Appendix).

C. Implementation

Starting from these conclusions, the optimal control has always a bang-bang structure. Numerical simulations in [19] show that for a classical aerocapture problem with ΔV minimization the vehicle flies nearly full lift up, then almost full lift down. Extending this result to this work, the control profile is

$$\sigma = \begin{cases} \sigma_0 & \text{when } t_0 < t \leq t_s \\ \sigma_d & \text{when } t_s < t < t_{\text{out}} \end{cases}$$

so from t_0 up to a switching time t_s the bank angle is small and equal to σ_0; then, from t_s to the atmosphere exit the control variable is equal to σ_d (Figure 9). Of course, a full-lift down trajectory is possible, if a switching time equal to 0 is obtained in the optimization process. Conversely, full-lift up cases can be found when t_s is higher with respect to the atmospheric exit time. As showed in [2], performances are not affected by the value of σ_0. For this reason, a fixed value of 5deg is selected for the initial bank angle.

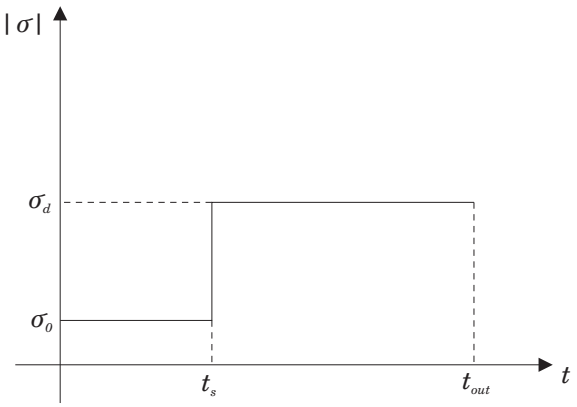

Fig. 9 Optimal bank angle profile

In conclusion, the aim is to find σ_d, t_s, α and f_0 that minimize the cost function

$$J = \varphi\left(\mathbf{x}\left(t_{\text{out}}\right),\ \alpha,\ f_0\right) = -m_0\left[1 - Kq^{\beta}\left(t_{\text{out}}\right)\right] e^{-\frac{\Delta V}{I_{\text{sp}} g_0}} \tag{43}$$

with

$$\Delta V = v_p^* - \left\|\mathbf{V}\left(t_{\text{fin}}\right)\right\| \tag{44}$$

such that

$$\dot{\mathbf{x}} = \begin{bmatrix} \dot{r} \\ \dot{V} \\ \dot{\gamma} \\ \dot{q} \end{bmatrix} = \begin{bmatrix} V \sin\gamma \\ -D - \frac{\mu_{\sigma^{\nearrow}}}{r^2} \sin\gamma \\ \frac{1}{V}\left[L\cos\sigma + \left(V^2 - \frac{\mu_{\sigma^{\nearrow}}}{r}\right)\frac{\cos\gamma}{r}\right] \\ f_q\left(r, V\right) \end{bmatrix} \tag{45}$$

where f_q is the explicit function describing the heat flux and with the bank angle

$$\sigma = \begin{cases} \sigma_0 & \text{when } t_0 < t \leq t_s \\ \sigma_d & \text{when } t_s < t < t_{\text{out}} \end{cases}$$

where t_{out} is the time when $r = r_{\text{int}}$, subjected to the final constraint

$$\left\|\mathbf{R}\left(t_{\text{fin}}\right)\right\| = r_p^* \tag{46}$$

where

$$\begin{bmatrix} \mathbf{R} \\ \mathbf{V} \end{bmatrix}_{t_{\text{fin}}} = \mathcal{M}_{\alpha,\ f_0}\left(r,\ V,\ \gamma\right)_{t_{\text{out}}} \tag{47}$$

with t_{fin} the time when the conditions

$$\begin{cases} \mathbf{V}\left(t_{\text{fin}}\right) \cdot \mathbf{R}\left(t_{\text{fin}}\right) = 0 \\ \frac{\mathrm{d}}{\mathrm{d}t}\left(\mathbf{V}\left(t_{\text{fin}}\right) \cdot \mathbf{R}\left(t_{\text{fin}}\right)\right) < 0 \end{cases} \tag{48}$$

already contained in $\mathcal{M}$, are attained. Eqs. (48) are the translation in P2-centered reference frame of the Eq. (27).

In addition, some inequality path constraints are included both on the load factor and on the dynamic pressure, in order

to avoid too high stresses on the structure, and also on the heating rate and the total heat load. These are

$$\begin{aligned} n = \sqrt{L^2 + D^2} \leq & n_{\max} \\ \bar{q} = \frac{1}{2}\rho V^2 \leq & \bar{q}_{\max} \\ \dot{q} \leq & \dot{q}_{\max} \\ q\left(t_{\text{out}}\right) \leq & q_{\max}\left(t_{\text{out}}\right) \end{aligned} \tag{49}$$

with $n_{\max} = 2.3$ g, $\bar{q}_{\max} = 4600$ Pa, $\dot{q}_{\max} = 460\ \text{W cm}^{-2}$ and $q_{\max}\left(t_{\text{out}}\right) = 70\ \text{kJ cm}^{-2}$, as in [15].

Since the cost function has multiple basins of attraction, this problem is solved using a MultiStart algorithm, adopting as local solver an *interior point method*. Ordinary differential equations are solved using an explicit $7^{\text{th}}/8^{\text{th}}$-order Runge-Kutta integration scheme with *regula falsi* as event function handler.

Eq. (25), describing the heat flux, is an implicit equation and its integration can be an issue, since at each step its root has to be found. However, it does not depend directly on the control variable and it is decoupled from the other three equations describing the dynamics. Hence, they can be solved separately and Eq. (25) can be integrated a-posteriori. Starting from this observation, the RK8 algorithm is used only to solve the ODEs related to r, V and γ; then for each computed couple $(\tilde{r}, \tilde{V})$ describing the trajectory, the equation

$$\dot{q} - k_0 \left(\frac{\rho}{r_n}\right)^{\frac{1}{2}} \tilde{V}^{3.04} \left(1 - \frac{c_{p_{\text{TPS}}} \left(\frac{\dot{q}}{\sigma \varepsilon}\right)^{\frac{1}{4}}}{H}\right) + C r_n^a \rho^b f(\tilde{V}) = 0 \tag{50}$$

is solved, allowing to compute $\dot{\tilde{q}}$ for each integration time. Then it is integrated using the trapezoidal rule. In conclusion, a wrap-up is needed in order to clearly represent how the optimization problem is solved. The block scheme in Figure 10 schematizes the logic flow followed in the optimization algorithm.

V. Results

Some reference final orbits are defined in order to show results and make comparisons. Sample final orbits around Mars with direct scientific interest have been chosen. They are shown in Table 3.

Table 3 Reference final orbits (r radius, h altitude, T period)

TAG	Target orbit	r [km]	h [km]	T [h]	Rationale
LMO	Low Mars Orbit	3690	300	1.89	Science
Ph	Phobos	9375	5985	7.66	Exploration
AS	Areostationary	20427	17037	24.62	TC/Weather
De	Deimos	23458	20068	30.30	Exploration

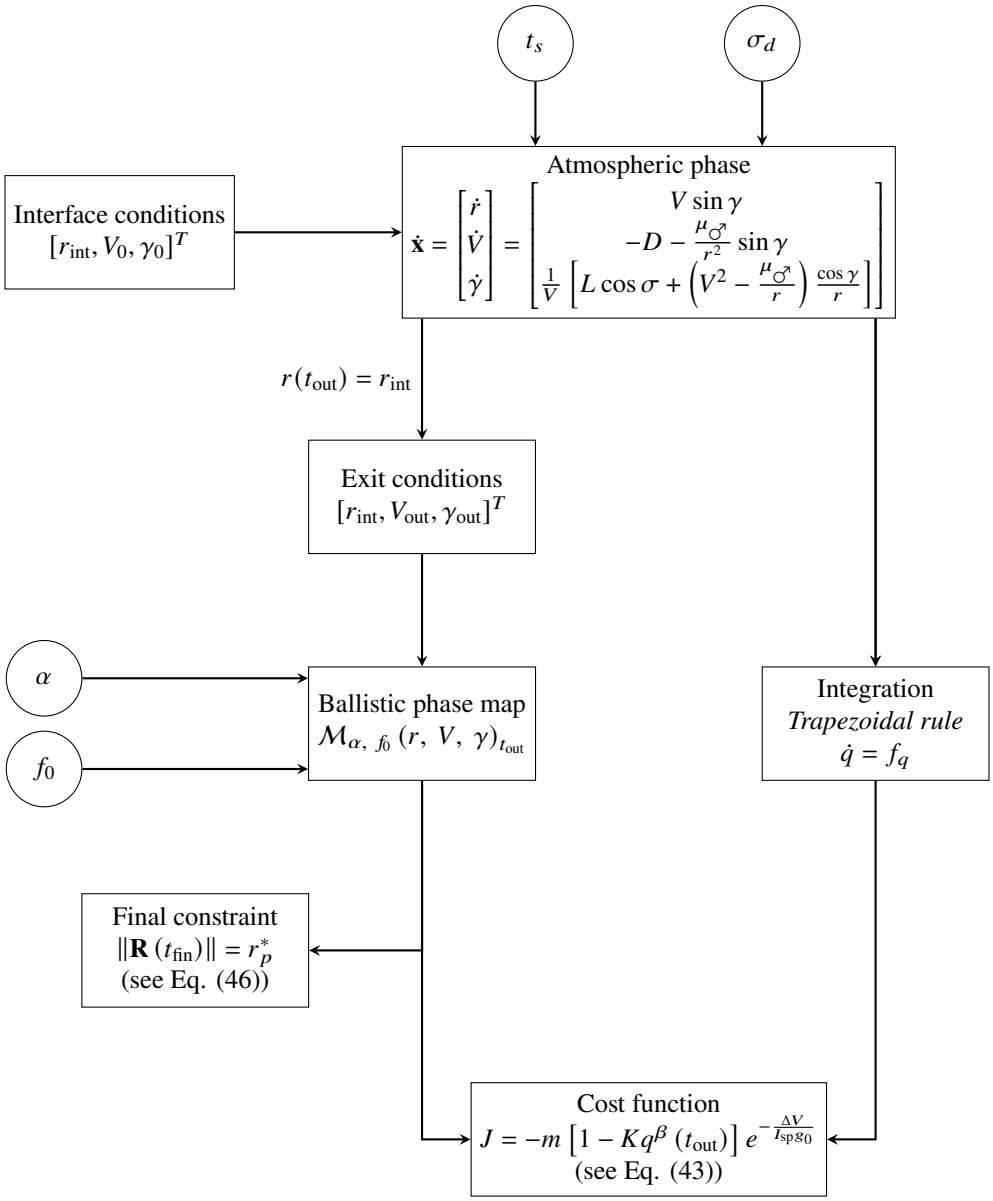

Fig. 10 Block scheme of the logic flow for solving the nonlinear programming problem.

A. Aero-ballistic capture solutions

Solutions related to aero-ballistic capture are shown first. Both the atmospheric phase and the ballistic phase are analyzed and presented in Table 4. t_{BAL} indicates the time of the ballistic phase, from the atmospheric exit up to the final orbit. The variables related to the atmospheric phase (t_s, σ_d) are similar even changing the final orbit radius. There is evidence that the atmospheric flight does not play a significant role, but the final state is attained due to a diverse ballistic trajectory. If the final orbit altitude is increased, the initial true anomaly decreases, because a stronger solar effect is needed. For the same reason, the transfer orbit apocenter has to be higher and so the ballistic time. Furthermore, the higher is the final orbit, the higher is the final mass, and so the aero-ballistic capture is more efficient for further orbits.

Table 4 Aero-ballistic capture solutions

TAG	t_s [s]	σ_d [deg]	α [deg]	f_0 [deg]	t_{out} [s]	t_{BAL} [d]	q [J/cm^2]	ΔV [km/s]	m_{fin} [kg]
LMO	13.4	64.4	199.2	51.56	338.4	10.33	9097	1.384	1274
Ph	6.68	61.41	346.58	1.51	334.78	41.21	8973	0.855	1509
AS	14.26	61	347.11	0.46	334.31	58.29	8955	0.564	1655
De	23.47	60.99	359.37	0.06	334.28	63.94	8955	0.523	1677

The aerostationary solution is taken as an example to make some observations. Figures 11(a)–11(d) illustrate the atmospheric path of the spacecraft in this solution. For what concerns velocity (Figure 11(b)), it is possible to notice that in the first seconds the spacecraft accelerates. Indeed, at the beginning of this phase the vehicle is approaching the pericenter of its orbit, so the velocity tends to increase, while at the same time the density of the atmosphere is still too low, and it is not able to counteract this phenomenon. Then, passing through denser layers of the atmosphere, the spacecraft slows down and it exits the atmosphere with a velocity of 4.92 km/s. Figure 12(a) shows the trajectory in synodic frame: it is a figure of eight and it has the apocenter in the II quadrant, as expected, because a raise in pericenter is sought. The orbit in inertial Mars-centered frame is depicted in Figure 12(b) and clearly shows this effect. The altitude profile in Figure 12(c) shows that the maximum distance reached by the spacecraft is 174 Martian radii. This distance is at the boundary of the Mars *sphere of influence*. In the Figure 12(d), the Mars-relative energy is plotted. At the end of the maneuver, the spacecraft has a higher orbital energy with respect to the initial time. This means that, remembering that the final point is the new pericenter by construction, an higher value for the pericenter distance is attained.

B. Aerocapture reference solutions

In order to understand if the aero-ballistic capture has some advantages on already known techniques, purely aerocapture solutions are derived for the study cases as well. These are taken as reference for comparison.
It can be proven that also for the standard aerocapture the optimal problem has a bang-bang control structure, but with only t_s and σ_d as parameters [2]. Table 5 summarizes relevant data for aerocapture. In this case, increasing the target orbit radius, the final bank angle, the atmospheric time and q (t_{out}) decrease, because less orbital energy has to be removed and converted into heat. Conversely, ΔV tends to increase, and so a lower final mass is obtained. In conclusion, it is possible to deduce that for final orbit close to the Mars surface, the aerocapture has better performances, but the further the spacecraft has to go, the more convenient the aero-ballistic capture becomes.

C. Fully propulsive maneuvers

A last analysis has to be done on trajectories using only propulsive maneuvers, in order to show their low efficiency with respect to aero-assisted methods [6]. Two different strategies of this kind are implemented:

1) *Direct insertion*: this is the typical method used today for Martian missions; the spacecraft is injected in the final

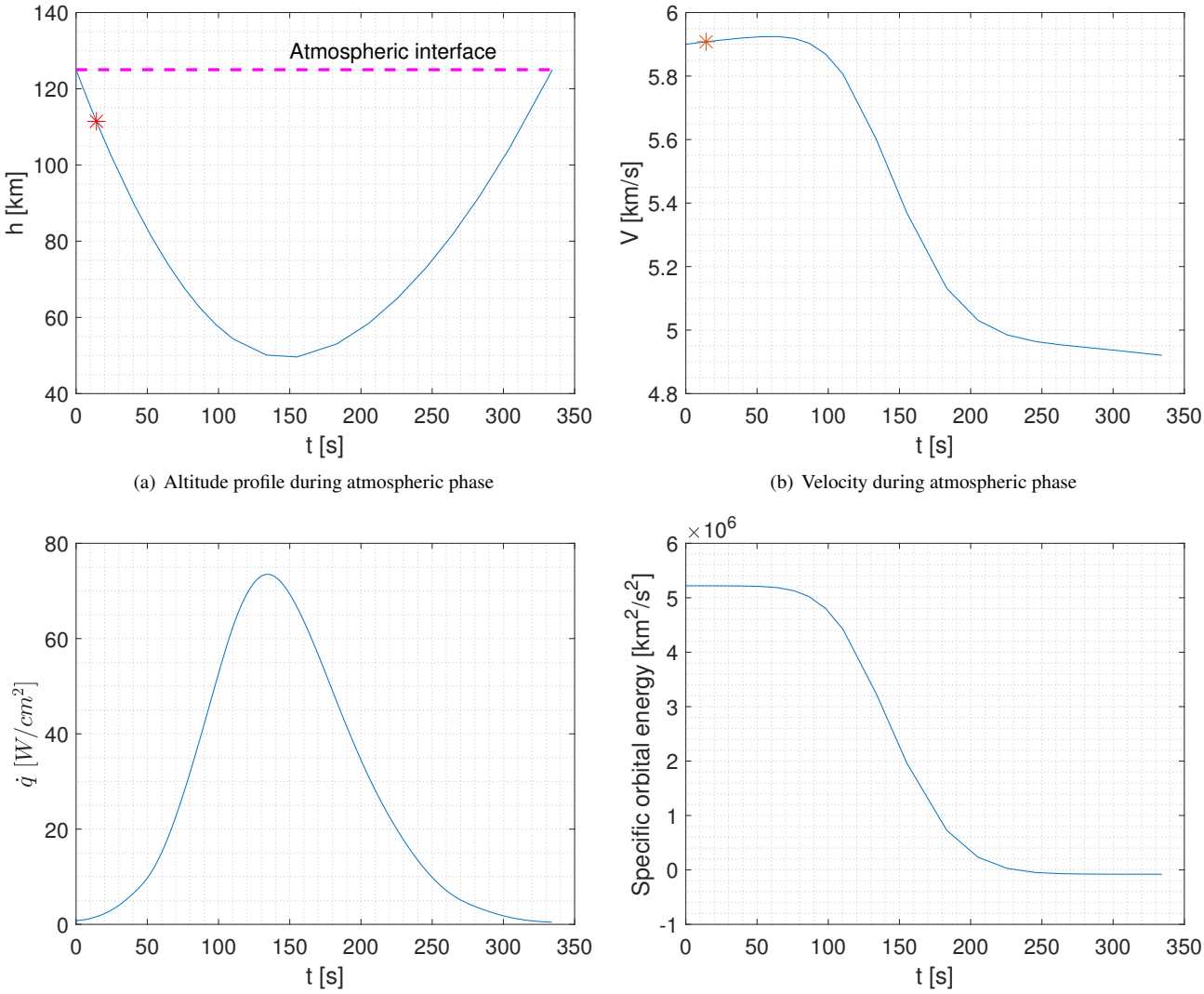

(a) Altitude profile during atmospheric phase

(b) Velocity during atmospheric phase

(c) Heat flux during atmospheric phase

(d) Mars-relative orbital energy

Fig. 11 Relevant quantities for the atmospheric phase of an aero-ballistic capture to an areostationary orbit. Asterisk indicates the switching time point.

Table 5 Aerocapture solutions

TAG	t_s [s]	σ_d [deg]	t_{out} [s]	t_{BAL} [h]	t_{fin} [h]	q (t_{out}) [J/cm^2]	ΔV [km/s]	m_{fin} [kg]
LMO	123.86	179	1427	0.44	0.83	17526	0.038	1868
Ph	1.71	98.06	454.49	2.08	2.2	11753	0.572	1624
AS	0	86.89	386.97	5.43	5.53	10472	0.671	1585
De	2.62	84.84	379.28	6.51	6.61	10299	0.668	1588

orbit directly from the hyperbolic trajectory, with a single impulse at the pericenter (Figure 13);

2) *Two-impulse maneuver*: this exploits both the Oberth effect and the solar gravity gradient. It is similar to the aero-ballistic capture, but instead of performing an atmospheric passage, the spacecraft is inserted on a transfer

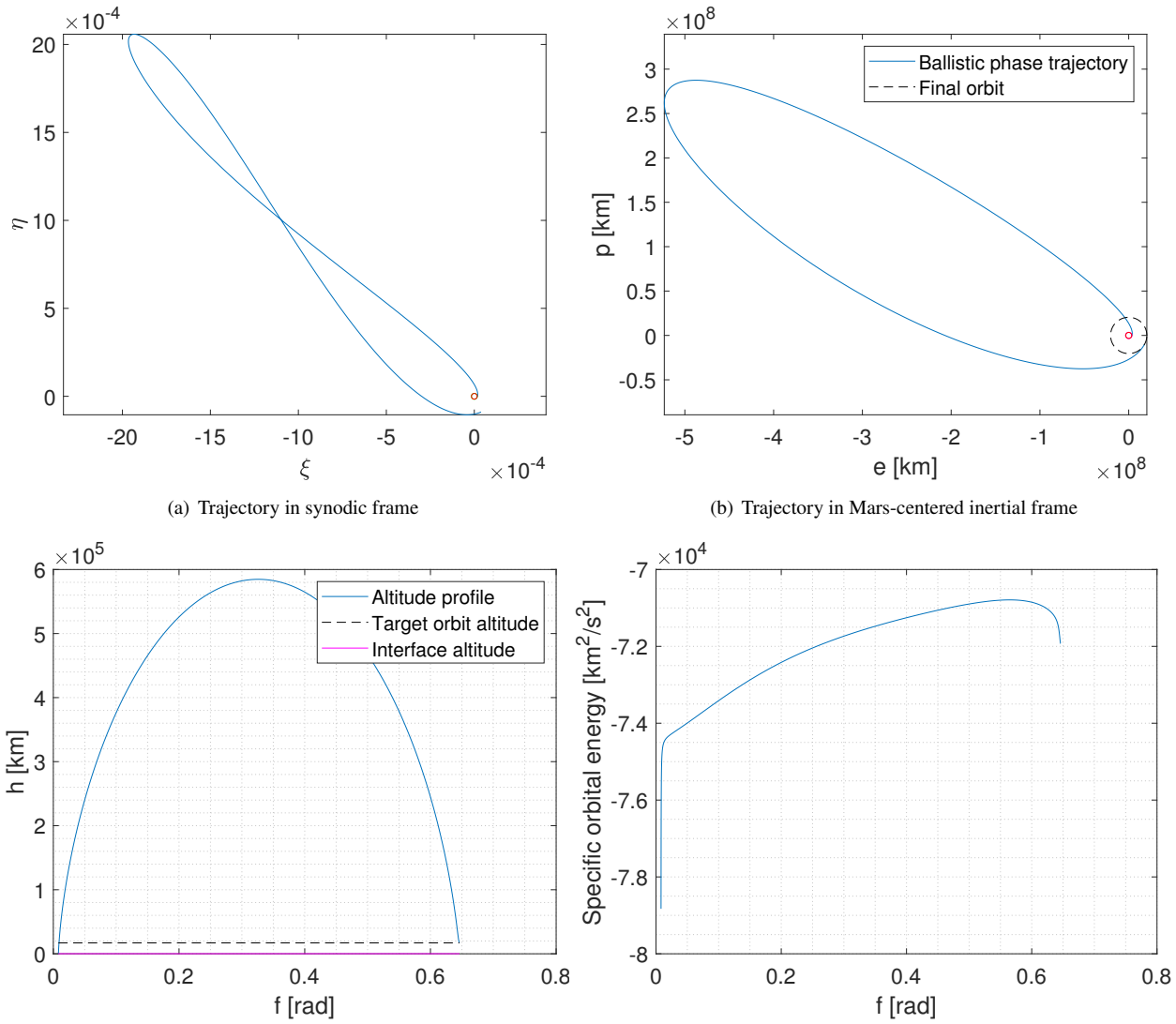

(a) Trajectory in synodic frame

(b) Trajectory in Mars-centered inertial frame

(c) Altitude profile during ballistic phase

(d) Mars-relative orbital energy

Fig. 12 Relevant quantities for the ballistic phase of an aero-ballistic capture to an areostationary orbit.

orbit with a high apocenter using a propulsive maneuver (Figure 14). Thus, this technique is defined as follows:

1) At the initial time, the spacecraft approaches Mars with an hyperbolic trajectory with the pericenter at a fixed altitude, outside the atmosphere. A conservative value of 200 km is selected;
2) At the pericenter of the hyperbolic trajectory, a first impulsive maneuvers is performed, in order to bring the spacecraft on a closed transfer orbit with a high apocenter;
3) The Sun gravity field accelerates the probe when it is far from Mars and, thus, the pericenter is naturally raised at the desired altitude;
4) Finally, a second propelled impulse is given a the pericenter in order to reduce the velocity and bring the apocenter to a prescribed value.

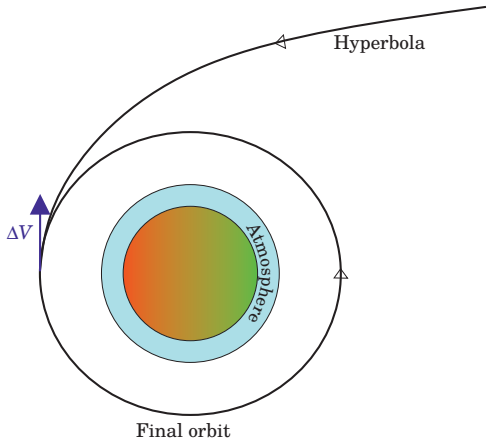

Fig. 13 Direct insertion: the spacecraft arrives on a *hyperbola* and a *single impulse* at its pericenter moves the probe to the *final orbit*.

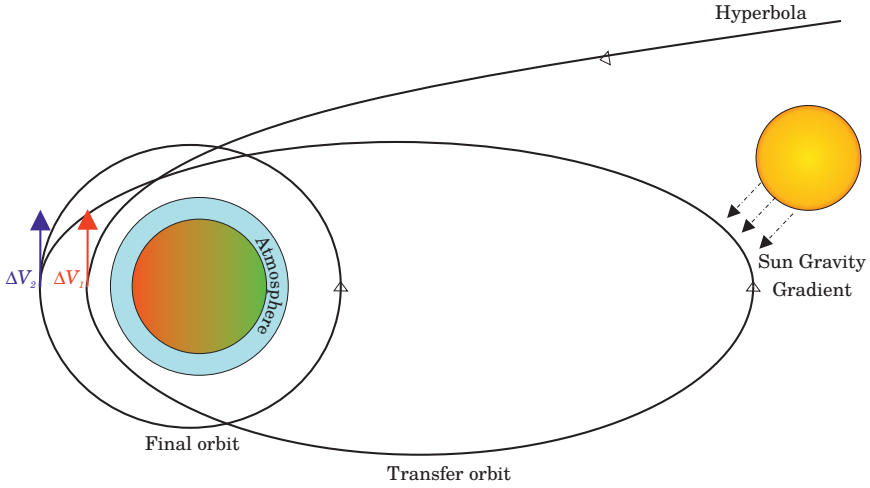

Fig. 14 The different phases of two-impulse maneuver: the spacecraft arrives on a *hyperbola*; then a *first impulse* at the pericenter brings the vehicle on a high elliptic transfer orbit; during the *ballistic phase* the solar gravity gradient raises the pericenter (dotted arrows); a *second impulse* is performed moving the probe to the *final orbit*.

Direct insertion was simply solved by evaluating the 2-body problem formulas. For the two-impulse maneuver an optimization problem similar to the aero-ballistic capture one is solved, with the velocity pericenter of the transfer orbit V_p, instead of the atmospheric phase parameters. Results for this two techniques are shown in Table 6. The two-impulse technique has always advantages in term of mass with respect to the direct insertion. However, both approaches have worse performances compared to the aero-assisted solutions.

D. General comparison

In order to understand when aero-ballistic capture is convenient with respect to aerocapture, a general comparison has to be performed. For this reason, some solutions are sought for both the aero-assisted problems for final circular orbits with altitudes from 200 km to 25000 km. In addition, solutions are computed also for fully propulsive maneuvers.

	Direct insertion		Two-impulse maneuver					
TAG	ΔV [km/s]	m_{fin} [kg]	α [deg]	f_0 [deg]	V_p [km/s]	ΔV_1 [km/s]	ΔV_2 [km/s]	m_{fin} [kg]
LMO	2.394	1030	138.11	355.19	4.829	1.027	1.355	1030
Ph	2.287	1062	115.26	341.27	4.876	0.989	0.856	1222
AS	2.378	1032	113.15	318.36	4.879	0.986	0.564	1343
De	2.403	1023	127.58	329.84	4.48	0.986	0.522	1361

Table 6 Fully propulsive maneuvers solutions

Results can be found in Figure 15. For lower orbits aerocapture is more efficient and the final mass is higher; but above 10000 km of altitude, aero-ballistic capture becomes the optimal solution in terms of mass delivered to the final orbit. The higher is the orbit, the more covenient is aero-ballistic capture. This result is achieved because both the total head load in the atmospheric phase and the needed propellant for the final orbit injection are lower. As already observed, fully propulsive solutions are very inefficient. It is important to notice that the diamond line solution, representing the single impulse maneuver, is actually the technique most used nowadays to close orbits about Mars.

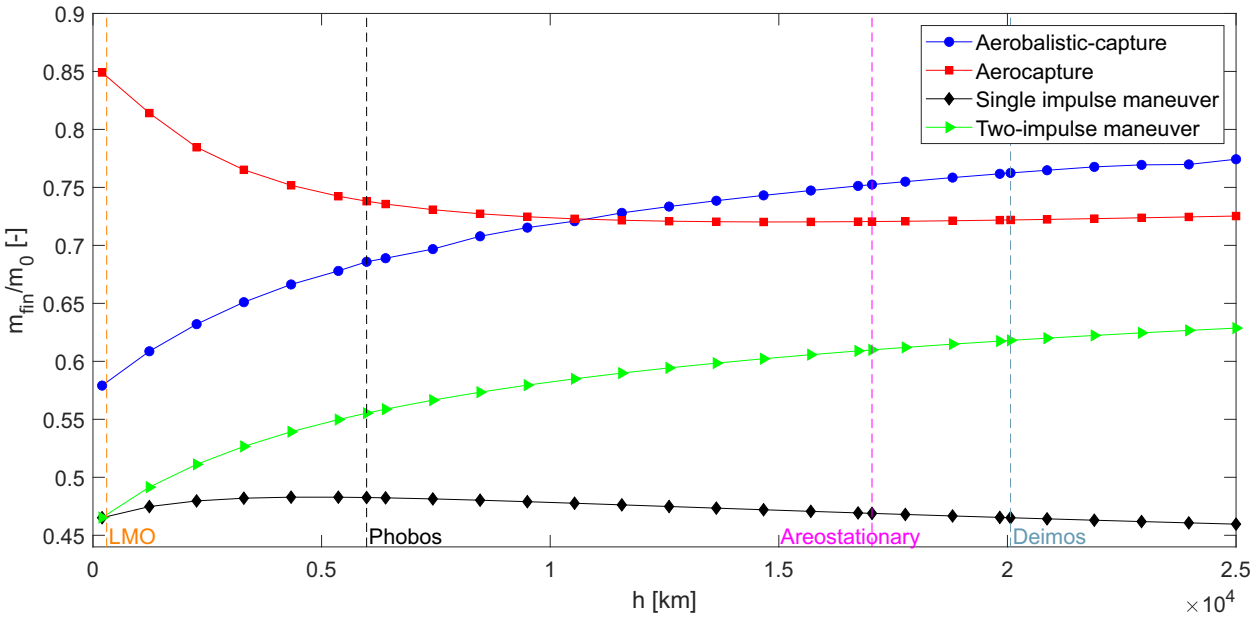

Fig. 15 Comparison of between aero-ballistic capture and aerocapture. Study cases orbits are reported in dashed lines.

VI. Conclusions

This paper elaborates a method which merges aerocapture and ballistic capture. This technique, called aero-ballistic capture, exploits the interaction of a spacecraft with the atmosphere, in order to remove energy thanks to friction. At the

exit from the atmosphere, the vehicle is on an elliptic orbit and the interaction with the solar gravity raises the pericenter of this transfer orbit up to a prescribed value. At the end, a propelled maneuver is performed in order to move the probe to its final orbit. It is shown that the optimal control for this problem has a bang-bang structure, allowing to solve it as a non-linear programming problem. Some study cases about Mars are analyzed, showing that trajectory is driven more by the ballistic phase than the atmospheric phase and the final mass increases, increasing the altitude of the final orbit. Comparison with aerocapture and fully propulsive maneuvers shows that aero-assisted maneuvers are always more efficient than fully propulsive approaches and aero-ballistic capture gives advantages in terms of final mass for high altitude orbits, when a final orbit with a radius bigger than 13400 km is targeted.

Appendix: Nonexistence of Singular optimal control

Here the nonexistence of the singular optimal control is proven. The Hamiltonian of the system in expanded form is

$$H = \lambda_0 \dot{\varphi} + \lambda_r V \sin\gamma + \lambda_V \left(-D - \frac{\mu_{\male} \sin\gamma}{r^2} \right) + + \lambda_\gamma \left(\frac{L}{V} \cos\sigma + \left(V^2 - \frac{\mu_{\male}}{r} \right) \frac{\cos\gamma}{rV} \right) + \lambda_q f_q \tag{51}$$

and the costate variables have to satisfy the equations

$$\dot{\lambda}_r = -\frac{\partial H}{\partial r} = \lambda_V \left(\frac{\partial D}{\partial r} - \frac{2\mu_{\male} \sin\gamma}{r^3} \right) - \lambda_\gamma \frac{\partial f_\gamma}{\partial r} - \lambda_q \frac{\partial f_q}{\partial r} \tag{52}$$

$$\dot{\lambda}_V = -\frac{\partial H}{\partial V} = -\lambda_r \sin\gamma + \lambda_V \frac{\partial D}{\partial V} - \lambda_\gamma \frac{\partial f_\gamma}{\partial V} - \lambda_q \frac{\partial f_q}{\partial V} \tag{53}$$

$$\dot{\lambda}_\gamma = -\frac{\partial H}{\partial \gamma} = -\lambda_r V \cos\gamma + \lambda_V \frac{\mu_{\male} \cos\gamma}{r^2} - \lambda_\gamma \frac{\partial f_\gamma}{\partial \gamma} \tag{54}$$

$$\dot{\lambda}_q = -\frac{\partial H}{\partial q} = 0 \tag{55}$$

$$\dot{\lambda}_0 = -\frac{\partial H}{\partial \varphi} = -\lambda_0 \frac{\partial \dot{\varphi}}{\partial \varphi} = 0 \tag{56}$$

where f_γ is the right-hand side of the Eq. (4c).

Since the cost function depends on some parameters, i.e., α and f_0, two additional transversal conditions are added [41]

$$\boldsymbol{\lambda}(t_{\text{out}})^T \int_{t_0}^{t_{\text{out}}} \frac{\partial \mathbf{f}}{\partial \alpha} \, \mathrm{d}t = 0 \tag{57}$$

$$\boldsymbol{\lambda}(t_{\text{out}})^T \int_{t_0}^{t_{\text{out}}} \frac{\partial \mathbf{f}}{\partial f_0} \, \mathrm{d}t = 0 \tag{58}$$

Since only the objective function depends on these parameters, Eq. (57) becomes

$$\lambda_0(t_{\text{out}}) \int_{t_0}^{t_{\text{out}}} \frac{\partial \dot{\varphi}}{\partial \alpha} \, \mathrm{d}t = 0 \quad \rightarrow \quad \lambda_0(t_{\text{out}}) \frac{\partial}{\partial \alpha} \int_{t_0}^{t_{\text{out}}} \frac{\mathrm{d}\varphi}{\mathrm{d}t} \, \mathrm{d}t = 0 \quad \rightarrow \quad \lambda_0(t_{\text{out}}) \frac{\partial \varphi(t_{\text{out}})}{\partial \alpha} = 0 \tag{59}$$

where the property that α is constant and does not depend on time is used. Similarly Eq. (58) becomes

$$\lambda_0(t_{\text{out}}) \frac{\partial \varphi(t_{\text{out}})}{\partial f_0} = 0 \tag{60}$$

The only condition satisfying Eqs. 59 and 60 is $\lambda_0(t_{\text{out}}) = 0$ and due to Eq. (56)

$$\lambda_0 \equiv 0 \quad \forall t \in [t_1,\ t_2] \tag{61}$$

Now, assuming by contradiction that the singular control exists, this means that $\lambda_\gamma = 0$ and $\dot{\lambda}_\gamma = 0$ in the time interval $[t_1,\ t_2] \subset [t_0,\ t_{\text{out}}]$. Simplifying Eq. (54) using these last assumptions, assuming that $\cos\gamma \neq 0$, it is found that

$$\lambda_r = \frac{\mu_{\sigma^{\prime}}}{r^2 V} \lambda_V \tag{62}$$

Then, by Maximum Principle, the relation

$$H = 0 \qquad \forall t \in [t_0,\ t_{\text{out}}] \tag{63}$$

has to hold on the optimal trajectory. This means, recalling that $\lambda_0 = 0$ and $\lambda_\gamma = 0$, that Eq. (51) becomes

$$\lambda_r V \sin\gamma - \lambda_V D - \lambda_V \frac{\mu_{\sigma^{\prime}} \sin\gamma}{r^2} + \lambda_q f_q = 0 \tag{64}$$

Inserting the Eq. (62) in this last expression, the result is

$$-\lambda_V D + \lambda_q f_q = 0 \tag{65}$$

Assuming that $\lambda_q \neq 0$, it is possible to write that

$$f_q = \frac{\lambda_V}{\lambda_q} D \tag{66}$$

Using this in Eqs. (52) and (53), the costate dynamics becomes

$$\dot{\lambda}_r = -\frac{2\mu_{\sun}\sin\gamma}{r^3}\lambda_V \tag{67}$$

$$\dot{\lambda}_V = -\lambda_r \sin\gamma \tag{68}$$

Now, starting from Eq. (62), the expression

$$\lambda_V = \frac{r^2 V}{\mu_{\sun}}\lambda_r \tag{69}$$

can be retrieved and, differentiating it with respect to the time, yields to

$$\dot{\lambda}_V = \frac{1}{\mu_{\sun}}\left(2r\dot{r}V\lambda_r + r^2\dot{V}\lambda_r + \dot{\lambda}_r r^2 V\right) \tag{70}$$

Putting Eq. (67) and the dynamics equations inside this equation, the result is

$$\dot{\lambda}_V = \frac{1}{\mu_{\sun}}\left[2rV^2\sin\gamma\lambda_r + r^2\left(-D - \frac{\mu_{\sun}\sin\gamma}{r^2}\right)\lambda_r - \frac{2\mu_{\sun}\sin\gamma}{r^3}r^2 V\lambda_V\right] \tag{71}$$

that can be simplified using Eq. (62), becoming

$$\dot{\lambda}_V = \left(-\frac{Dr^2}{\mu_{\sun}} - \sin\gamma\right)\lambda_r \tag{72}$$

This last equation has an extra non-null term with respect to Eq. (68) . The only way to have Eq. (68) consistent with Eq. (72) is that $\lambda_r = 0$. This means that also $\lambda_V = 0$. And, consequentially, $f_q = 0$; but this is a non-sense.

Otherwise, if $\lambda_q = 0$, Eq. (65) is simply

$$-\lambda_V D = 0 \rightarrow \lambda_V = 0 \tag{73}$$

since $D \neq 0$ always in the trajectory. But $\lambda_V = 0$ together with Eq. (62) indicates that $\lambda_r = 0$. Therefore, the costate vector $\boldsymbol{\lambda} = [\lambda_0, \lambda_r,\ \lambda_V,\ \lambda_\gamma,\ \lambda_q]^T = \mathbf{0}$ in $[t_1,\ t_2]$. Since that the costate equations are affine in $\boldsymbol{\lambda}$ and $\boldsymbol{\lambda}$ is continuous in $[t_0,\ t_{\text{out}}]$, it follows that $\boldsymbol{\lambda} = \mathbf{0}, \quad \forall t \in [t_0,\ t_{\text{out}}]$; but this is not possible because it is in contradiction with the Maximum Principle that states that the costate vector cannot be null. Thus, the possibility to have a singular optimal control in the optimal aero-ballistic capture problem is ruled out.

References

[1] Salotti, J.-M., and Heidmann, R., "Roadmap to a human Mars mission," *Acta Astronautica*, Vol. 104, No. 2, 2014, pp. 558–564. https://doi.org/10.1016/j.actaastro.2014.06.038.

[2] Lu, P., Cerimele, C. J., Tigges, M. A., and Matz, D. A., "Optimal Aerocapture Guidance," *Journal of Guidance, Control, and Dynamics*, Vol. 38, No. 4, 2015, pp. 553–565. https://doi.org/10.2514/1.G000713.

[3] Repic, E. M., Boobar, M. G., and Chapel, F. G., "Aerobraking as a potential planetary capture mode," *Journal of Spacecraft and Rockets*, Vol. 5, No. 8, 1968, pp. 921–926. https://doi.org/10.2514/3.29389.

[4] French, J. R., and Cruz, M. I., "Aerobraking and aerocapture for planetary missions," *Astronautics & Aeronautics*, Vol. 18, No. 2, 1980, pp. 48–55, 71.

[5] Walberg, G. D., "A Survey of Aeroassisted Orbit Transfer," *Journal of Spacecraft and Rockets*, Vol. 22, No. 1, 1985, pp. 3–18. https://doi.org/10.2514/3.25704.

[6] Hall, J. L., Noca, M. A., and Bailey, R. W., "Cost-Benefit Analysis of the Aerocapture Mission Set," *Journal of Spacecraft and Rockets*, Vol. 42, No. 2, 2005, pp. 309–320. https://doi.org/10.2514/1.4118.

[7] Lockwood, M. K., "Titan aerocapture systems analysis," *39th AIAA/ASME/SAE/ASEE Joint Propulsion Conference and Exhibit*, 2003, p. 4799. https://doi.org/10.2514/6.2003-4799.

[8] Takashima, N., Hollis, B. R., Vincent Zoby, E., Sutton, K., Olejniczak, J., Wright, M. J., and Prabhu, D., "Preliminary Aerothermodynamics of Titan Aerocapture Aeroshell," *39th AIAA/ASME/SAE/ASEE Joint Propulsion Conference and Exhibit*, 2003. https://doi.org/10.2514/6.2003-4952.

[9] Starr, B. R., and Westhelle, C. H., "Aerocapture Performance Analysis of a Venus Exploration Mission," *AIAA Atmospheric Flight Mechanics Conference and Exhibit*, Vol. 1, 2005, pp. 435–448. https://doi.org/10.2514/6.2005-5913.

[10] Lockwood, M. K., "Neptune Aerocapture Systems Analysis," *AIAA Atmospheric Flight Mechanics Conference and Exhibit*, 2004, pp. 660–675. https://doi.org/10.2514/6.2004-4951.

[11] Lafleur, J. M., "The Conditional Equivalence of ΔV Minimization and Apoapsis Targeting in Numerical Predictor-Corrector Aerocapture Guidance," *NASA TM-2011-216156*, 2011.

[12] Vaughan, D., Miller, H. C., Griffin, B., James, B. F., and Munk, M. M., "A Comparative Study of Aerocapture Missions with a Mars Destination," *41st AIAA/ASME/SAE/ASEE Joint Propulsion Conference and Exhibit*, 2005. https://doi.org/10.2514/6.2005-4110.

[13] Fraysse, H., Powell, R., Rousseau, S., and Striepe, S., "CNES-NASA Studies of the Mars Sample Return Orbiter Aerocapture Phase," *51st International Astronautical Congress*, 2000.

[14] Hamel, J.-F., and Lafontaine, J. D., "Improvement to the Analytical Predictor-Corrector Guidance Algorithm Applied to Mars Aerocapture," *Journal of Guidance, Control, and Dynamics*, Vol. 29, No. 4, 2006, pp. 1019–1022. https://doi.org/10.2514/1.20126.

[15] Masciarelli, J. P., Rousseau, S., Fraysse, H., and Perot, E., "An analytic aerocapture guidance algorithm for the Mars Sample Return Orbiter," *Atmospheric Flight Mechanics Conference*, 2000. https://doi.org/10.2514/6.2000-4116.

[16] Powell, R., Willcockson, W., and Johnson, M., "Numerical Roll Reversal Predictor Corrector Aerocapture and Precision Landing Guidance Algorithms for the Mars Surveyor Program 2001 Missions," *23rd AIAA Atmospheric Flight Mechanics Conference*, 1998. https://doi.org/10.2514/6.1998-4574.

[17] Ro, T. U., and Queen, E. M., "Study of Martian Aerocapture Terminal Point Guidance," *23rd AIAA Atmospheric Flight Mechanics Conference*, 1998. https://doi.org/10.2514/6.1998-4571.

[18] Kozynchenko, A. I., "Development of optimal and robust predictive guidance technique for Mars aerocapture," *Aerospace Science and Technology*, Vol. 30, No. 1, 2013, pp. 150–162. https://doi.org/10.1016/j.ast.2013.07.012.

[19] Miele, A., Wang, T., Lee, W., and Zhao, Z., "Optimal trajectories for the aeroassisted flight experiment," *Acta Astronautica*, Vol. 21, No. 11-12, 1990, pp. 735–747. https://doi.org/10.1016/0094-5765(90)90116-3.

[20] Belbruno, E. A., and Miller, J. K., "Sun-Perturbed Earth-to-Moon Transfers with Ballistic Capture," *Journal of Guidance, Control, and Dynamics*, Vol. 16, No. 4, 1993, pp. 770–775. https://doi.org/10.2514/3.21079.

[21] Topputo, F., and Belbruno, E., "Computation of weak stability boundaries: Sun-Jupiter system," *Celestial Mechanics and Dynamical Astronomy*, Vol. 105, No. 1, 2009, pp. 3–17. https://doi.org/10.1007/s10569-009-9222-5.

[22] Hyeraci, N., and Topputo, F., "Method to Design Ballistic Capture in the Elliptic Restricted Three-Body Problem," *Journal of Guidance, Control, and Dynamics*, Vol. 33, No. 6, 2010, pp. 1814–1823. https://doi.org/10.2514/1.49263.

[23] Hyeraci, N., and Topputo, F., "The role of true anomaly in ballistic capture," *Celestial Mechanics and Dynamical Astronomy*, Vol. 116, No. 2, 2013, pp. 175–193. https://doi.org/10.1007/s10569-013-9481-z.

[24] Luo, Z., Topputo, F., Bernelli-Zazzera, F., and Tang, G., "Constructing ballistic capture orbits in the real Solar System model," *Celestial Mechanics and Dynamical Astronomy*, Vol. 120, No. 4, 2014, pp. 433–450. https://doi.org/10.1007/s10569-014-9580-5.

[25] Luo, Z., and Topputo, F., "Capability of satellite-aided ballistic capture," *Communications in Nonlinear Science and Numerical Simulation*, Vol. 48, 2017, pp. 211–223. https://doi.org/10.1016/j.cnsns.2016.12.021.

[26] Luo, Z., and Topputo, F., "Analysis of ballistic capture in Sun-planet models," *Advances in Space Research*, Vol. 56, No. 6, 2015, pp. 1030–1041. https://doi.org/10.1016/j.asr.2015.05.042.

[27] Circi, C., and Teofilatto, P., "On the Dynamics of Weak Stability Boundary Lunar Transfers," *Celestial Mechanics and Dynamical Astronomy*, Vol. 79, No. 1, 2001, pp. 41–72. https://doi.org/10.1023/A:1011153610564.

[28] Yamakawa, H., Kawaguchi, J., Ishii, N., and Matsuo, H., "On Earth-Moon transfer trajectory with gravitational capture," *Advances in the Astronautical Sciences*, Vol. 85, 1993, pp. 397–416.

[29] Yamakawa, H., Kawaguchi, J., Ishii, N., and Matsuo, H., "Numerical study of gravitational capture orbit in the Earth-Moon system," *Advances in the Astronautical Sciences*, Vol. 79, 1992, pp. 1113–1132.

[30] Huang, T.-Y., and Innanen, K., "The gravitational escape/capture of planetary satellites," *The Astronomical Journal*, Vol. 88, 1983, pp. 1537–1548.

[31] Luo, Z.-F., and Topputo, F., "Mars orbit insertion via ballistic capture and aerobraking," *Astrodynamics*, Vol. 5, No. 2, 2021, pp. 167–181. https://doi.org/10.1007/s42064-020-0095-4.

[32] Wright, M. J., Beck, R. A., Edquist, K. T., Driver, D., Sepka, S. A., Slimko, E. M., and Willcockson, W. H., "Sizing and Margins Assessment of Mars Science Laboratory Aeroshell Thermal Protection System," *Journal of Spacecraft and Rockets*, Vol. 51, No. 4, 2014, pp. 1125–1138. https://doi.org/10.2514/1.A32579.

[33] Justus, C. G., and Braun, R. D., "Atmospheric Environments for Entry, Descent and Landing (EDL)," *Technical report, NASA Marshall Space Flight Center*, 2007.

[34] Pitts, D., Tillman, J., Johnson, N., Murphy, J., Pollack, J., Colbum, D., Haberle, R., Zurek, R., and Stewart, I., "The Mars Atmosphere: Observations and Model Profiles for Mars Missions," *NASA JSC-24455*, 1990.

[35] Curtis, H. D., *Orbital Mechanics for Engineering Students*, Butterworth-Heinemann, 2013. https://doi.org/10.1016/C2011-0-69685-1, Chap. 12.

[36] Olynick, D., Loomis, M., Chen, Y. ., Venkatapathy, E., and Allen, G., "New TPS design strategies for planetary entry vehicle design," *37th Aerospace Sciences Meeting and Exhibit*, 1999. https://doi.org/10.2514/6.1999-348.

[37] Tauber, M. E., Bowles, J. V., and Yang, L., "Use of atmospheric braking during Mars missions," *Journal of Spacecraft and Rockets*, Vol. 27, No. 5, 1990, pp. 514–521. https://doi.org/10.2514/3.26174.

[38] Tauber, M. E., and Sutton, K., "Stagnation-point radiative heating relations for Earth and Mars entries," *Journal of Spacecraft and Rockets*, Vol. 28, No. 1, 1991, pp. 40–42. https://doi.org/10.2514/3.26206.

[39] Korzun, A. M., Dubos, G. F., Iwata, C. K., Stahl, B. A., and Quicksall, J. J., "A concept for the Entry, Descent, and Landing of high-mass payloads at Mars," *Acta Astronautica*, Vol. 66, No. 7-8, 2010, pp. 1146–1159. https://doi.org/10.1016/j.actaastro.2009.10.003.

[40] Szebehely, V., *Theory of Orbit: The Restricted Problem of Three Bodies*, Elsevier, 1968. Pages 354–357.

[41] Pontryagin, L., Boltyanskii, V., and Gamkrelidze, R., *The Mathematical Theory of Optimal Processes*, John Wiley & Sons, 1962. Pages 191–197.

[42] Longuski, J. M., Guzmán, J. J., and Prussing, J. E., *Optimal Control with Aerospace Applications*, Vol. 32, Springer Science & Business Media, 2013. Pages 26–28.